nature communications

Article

https://doi.org/10.1038/s41467-024-53100-z

Coronavirus M protein promotes mitophagy over virophagy by recruiting PDPK1 to phosphorylate SQSTM1 at T138

Received: 18 January 2024

Accepted: 1 October 2024

Published online: 16 October 2024

Check for updates

Yahui Li[1,2,5], Chunyan Li[1,5], Chenchen Zhao[1,5], Jiayu Wu[1], Ya Zhu[1], Fei Wang[1], Jiepeng Zhong[1], Yan Yan[1], Yulan Jin[1], Weiren Dong[1], Jinyang Chen[1], Xianghong Yang[3], Jiyong Zhou[1,4] ✉ & Boli Hu[1] ✉

Autophagy plays a dual role in coronavirus infection, facilitating the elimination of either proviral components (virophagy) or antiviral factors such as mitochondria (mitophagy), leading to complex mechanisms of immune evasion. Understanding the mechanisms that govern the switch between the autophagic degradation of deleterious or beneficial substrates in coronavirus infection is crucial for developing precise drug targets to treat virus-induced diseases. However, this switch remains largely unknown. Using a dual split-fluorescence assay, we identify PDPK1 as a negative regulator of innate immunity, directing the transition from virophagy to mitophagy through the phosphorylation of SQSTM1 at T138. Remarkably, a PDPK1-targeting peptide inhibits the replication of various RNA viruses by restoring innate immunity through enhanced virophagy and suppressed mitophagy, thereby protecting female mice from lethal infections. These findings underscore the detrimental role of PDPK1 in innate immunity by orchestrating the shift from virophagy to mitophagy, positioning PDPK1 as a promising pharmacological target for effectively combating a broad spectrum of virus infections.

Coronaviruses are a group of viruses capable of causing severe and often fatal diseases in humans and animals, primarily due to their ability to evade host immune responses[1–3]. These viruses frequently manipulate the autophagy process to suppress host immune defenses and enhance their replication efficiency. Autophagy is a cellular mechanism that degrades and recycles damaged organelles, proteins, and invading pathogens. This includes selective degradation pathways like mitophagy, which targets mitochondria[4–10], and virophagy, which targets viral particles[5,11–14]. Viruses exploit mitophagy to degrade mitochondria and suppress host innate immune signaling, while host cells attempt to eliminate viruses through virophagy.

In the complex interplay between viruses and host cells, identifying key molecules that regulate both antiviral and proviral autophagy is crucial for enhancing host defenses and preventing viruses from exploiting autophagic pathways. SQSTM1 is a well-known autophagy cargo receptor (ACR) that plays a dual role during pathogen infection[15–19]. It can promote the degradation of viral proteins, aiding in the elimination of the virus, but can also be manipulated by viruses to promote mitochondrial degradation, thereby suppressing immune responses.

In this study, we found that SQSTM1 promoted the degradation of coronavirus (CoV) M proteins, infectious bursal disease virus (IBDV) VP2 and influenza A virus (IAV) PB1-F2, as well as mitochondria. As a

[1]MOA Key Laboratory of Animal Virology, Zhejiang University Center for Veterinary Sciences, Hangzhou, China. [2]Clinical Research Institute, Zhejiang Provincial People's Hospital, Affiliated People's Hospital, Hangzhou Medical College, Hangzhou, China. [3]Emergency and Critical Care Center, Intensive Care Unit, Zhejiang Provincial People's Hospital, Affiliated People's Hospital, Hangzhou Medical College, Hangzhou, China. [4]State Key Laboratory for Diagnosis and Treatment of Infectious Diseases, First Affiliated Hospital, Zhejiang University, Hangzhou, China. [5]These authors contributed equally: Yahui Li, Chunyan Li, Chenchen Zhao. ✉e-mail: jyzhou@zju.edu.cn; Bolihu@zju.edu.cn

method to investigate the presence of a key regulator capable of mediating the switch between virophagy and mitophagy, we developed a dual-split-fluorescence assay to monitor the binding of SQSTM1 to either the M protein or mitochondria. Based on the assay results, PDPK1 emerged as a central player redirecting the binding of SQSTM1 from the M protein to mitochondria. This redirection aids immune evasion by preventing virophagy and promoting mitophagy. A PDPK1-targeting peptide effectively eliminated CoV, IBDV and IAV by restoring virophagy and inhibiting mitophagy, ultimately protecting mice from lethal infection. These findings provide a promising drug target for future virus treatments and a reference research model for the dual functionality of autophagy and drug targets in studies of other diseases.

Results

Coronavirus M protein is degraded by SQSTM1-dependent autophagy

Since SQSTM1 extensively recognizes numerous viral proteins, we investigated whether SQSTM1 also interacts with M proteins from coronaviruses. Co-IP assays revealed that PEDV M, SARS M, IBV M and PDCoV M, which are from the four distinct genera of coronavirus (α, β, γ, and δ, respectively), interacted with SQSTM1 (Figs. 1A and S1A).

Alignment (Fig. S1B) and co-IP analysis revealed that M mutants lacking the CD region (GFP-MΔCD$\beta_{1\text{-}5}$ and GFP-MΔCD) lost the ability to precipitate SQSTM1 (Fig. 1B, C). A split $GFP_{1–10/11}$ fluorescent reporter assay was used to compare the strength of the interaction (Fig. 1D), and the results revealed that, in the presence of GFP_{11}-SQSTM1, M-CDs-$GFP_{1\text{-}10}$ (CDs of M proteins from the 4 distinct genera) emitted a stronger split $GFP_{1\text{-}10/11}$ signal than did the full-length M or MΔCD (Figs. 1E, F, S1C and S1D). Microscale thermophoresis (MST) assays revealed that M-CD bound to SQSTM1 with greater binding affinity (0.115 ± 0.028 μM) than did full-length M (3.54 ± 2.076 μM) (Fig. 1G), whereas MΔCD lost the ability to bind with SQSTM1 (227.77 μM). The above data indicated that the CD region was responsible for the interaction of the M proteins with SQSTM1.

Next, we found that GFP-M was precipitated from cells harboring either Flag-SQSTM1 or Flag-SQSTM1ΔUBA (lacking the ubiquitin-associated domain) (Fig. S1E). In addition, a GST pull-down assay indicated a direct interaction between SQSTM1 and M (Fig. S1F). The above results confirmed the ubiquitin-independent interaction between SQSTM1 and M.

We then investigated whether M was degraded through SQSTM1-dependent autophagy. The autophagy inhibitors chloroquine (CQ) and wortmannin (Wor.) rescued the decrease in M protein levels induced by SQSTM1 (Fig. S1G). Similarly, *SQSTM1* KO increased the levels of GFP-M and GFP-M-CD but not those of GFP or GFP-MΔCD (Fig. 1H). Confocal microscopy analysis revealed that SQSTM1 expression increased the colocalization of LC3B with GFP-M or GFP-M-CD but not with GFP-MΔCD (Fig. 1I), indicating that M-CD was critical for M localization to autophagosomes.

Similarly, SQSTM1 facilitated the degradation of IBDV VP2 and H1N1 PB1-F2 by interacting with them (Fig. S1H-S1J).

These data indicated that SQSTM1 regulated the autophagic degradation of M, as well as IBDV VP2 and H1N1 PB1-F2.

PDPK1 attenuates M degradation by retargeting SQSTM1 to mitochondria

A previous study showed that the M protein promotes mitophagy[20]. We next investigated whether the M protein promotes the binding of SQSTM1 to mitochondria. PEDV infection and PM or M protein expression promoted the colocalization of SQSTM1 with mitochondria (Fig. S2A). TOMM22, a mitochondrial outer membrane protein, was subsequently shown to interact with SQSTM1 via mass spectrometry analysis (Fig. S2B and S2C). A GST pull-down assay confirmed the direct interaction between SQSTM1 and TOMM22 (Fig. S2D).

A model was designed using dual split fluorescent reporters, namely, $GFP_{1–10/11}$ and $sfCherry2_{1–10/11}$, to track the targeting of SQSTM1 to the M protein or mitochondria (Fig. 2A). The main kinases responsible for regulating the interaction between SQSTM1 and M or TOMM22 were screened (Figs. 2B, C, S2E, and S2F). Compared with dimethyl sulfoxide (DMSO), a PDPK1 inhibitor (OSU-03012) produced the strongest intensity of the $GFP_{1\text{-}10/11}$ signal ($P < 0.0001$) and the weakest intensity of the $sfCherry2_{1\text{-}10/11}$ signal ($P = 0.0003$), suggesting that inhibition of PDPK1 redirected the targeting of SQSTM1 from mitochondria to the M protein.

We next evaluated the role of PDPK1 in the interaction between SQSTM1 and M or TOMM22. *PDPK1* KO decreased the intensity of the $sfCherry2_{1\text{-}10/11}$ signal, and increased the intensity of the $GFP_{1\text{-}10/11}$ signal, and rescue of PDPK1 expression restored the fluorescence of $sfCherry2_{1\text{-}10/11}$ and $GFP_{1\text{-}10/11}$ (Fig. 2D, E). Consistently, rescuing PDPK1 expression in the *PDPK1*-KO cell line increased the interaction between SQSTM1 and endogenous TOMM22, and decreased the binding of SQSTM1 to M (Fig. 2F). Conversely, OSU-03012 treatment at a concentration of 2 μM increased the binding of SQSTM1 to M but decreased its binding to TOMM22 (Fig. S2G-S2I), confirming that PDPK1 redirected SQSTM1 from M to TOMM22.

We next investigated whether PDPK1 regulated M protein or mitochondrial degradation. SQSTM1 expression substantially decreased the M and TOMM22 levels in *SQSTM1*-KO cells compared with those in control cells (Fig. S2J), and OSU-03012 treatment further decreased the M levels but restored the TOMM22 levels compared with those in the control group. In contrast, SQSTM1 expression decreased the level of M but not the level of TOMM22 in *PDPK1*-KO cells (Fig. 2G); additionally, restoring PDPK1 expression in these cells restored M expression but conversely decreased TOMM22 levels. Moreover, CQ or wortmannin treatment completely abolished the effects of SQSTM1 on M and TOMM22 degradation even in the presence of PDPK1, whereas Mdivi-1, a mitophagy-specific inhibitor, only blocked the effect of SQSTM1 on TOMM22 degradation but not M degradation (Fig. 2G). Next, a cycloheximide (CHX) chase assay showed that knocking out *PDPK1* promoted M degradation but inhibited TOMM22 degradation and that restoring PDPK1 expression reversed these effects (Fig. S2K). A tandem reporter construct encoding an RFP-GFP-tagged mitochondrion-targeting signal sequence, namely, RFP-GFP-Mito, was used to track mitophagy[21]., Compared with EV transfection, SQSTM1 expression led to a great decrease in the GFP signal but not the RFP signal, while *PDPK1* KO and OSU treatment reversed the decrease in GFP fluorescence (Fig. 2H). These data indicated that PDPK1 inhibited M degradation but promoted mitochondrial degradation.

In summary, PDPK1 attenuated M degradation by translocating SQSTM1 to mitochondria (Fig. 2I).

PDPK1 directly phosphorylates T138 of SQSTM1

We next wondered whether M interacts with PDPK1. M mutants lacking $\beta_{3\text{-}5}$ (GFP-MΔCD$\beta_{1\text{-}5}$ and GFP-MΔ$\beta_{3\text{-}5}$), but not other truncated forms of M, lost the ability to interact with PDPK1, suggesting that M indeed interacted with PDPK1 through M-$\beta_{3\text{-}5}$ (Fig. 3A). Anti-PDPK1 immunoprecipitation of PEDV-infected cell lysates confirmed the interaction of endogenous PDPK1 with the M protein (Fig. S3A). A split $GFP_{1\text{-}10/11}$ fluorescence assay indicated that M-$\beta_{3\text{-}5}$-$GFP_{1\text{-}10}$ from various coronaviruses presented stronger $GFP_{1\text{-}10/11}$ fluorescence with GFP_{11}-PDPK1 than M-$GFP_{1\text{-}10}$ did (Fig. S3B and S3C). A GST pull-down assay confirmed the direct binding of M or M-$\beta_{3\text{-}5}$ to TOMM22 (Fig. S3D). Consistently, MST assays showed that M-$\beta_{3\text{-}5}$ obviously bound to PDPK1 with greater binding affinity (0.071 ± 0.124 μM) than did full-length M (0.944 ± 1.346 μM) and MΔ$\beta_{3\text{-}5}$ (37.795 μM) (Fig. 3B). Similarly, we found that the $\beta_{3\text{-}5}$ motif is highly conserved in both IBDV VP2 and H1N1 PB1-F2 (Fig. S3E). Additionally, VP2 and PB1-F2 interacted with

https://doi.org/10.1038/s41467-024-53100-z

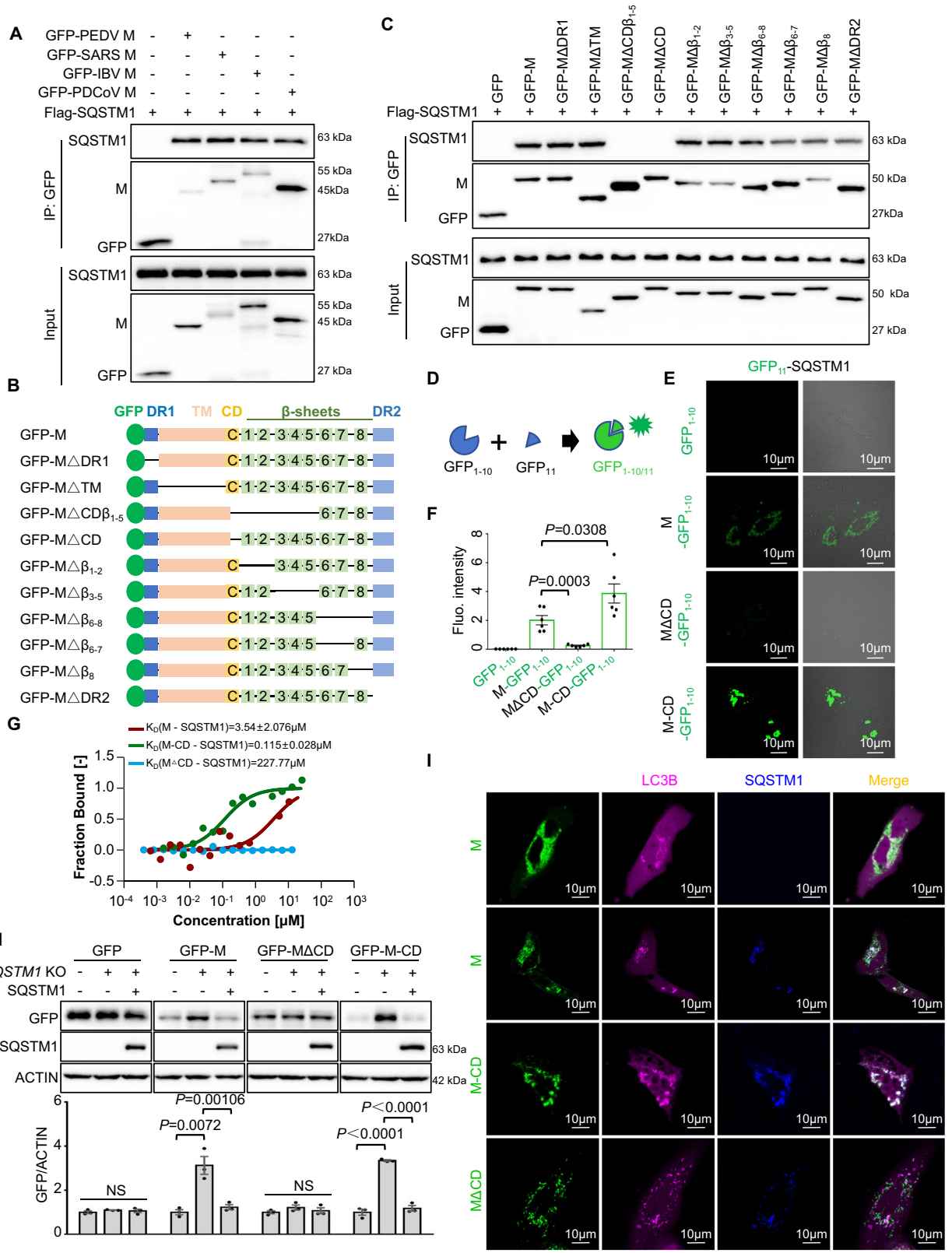

PDPK1 through this conserved motif, which is termed as PDPK1 Interaction Region (PIR) (Fig. S3F and S3G).

We next wondered whether M regulates the interaction between SQSTM1 and PDPK1. Anti-Flag-SQSTM1 IP and a GST pull-down assay confirmed the direct interaction between SQSTM1 and PDPK1 (Figs. 3C and S3H). Moreover, M-$GFP_{1\text{-}10}$, GFP-PM, or PEDV infection enhanced the interaction between PDPK1 and SQSTM1 (Figs. 3C–E and S3I). However, compared with that of $GFP_{1\text{-}10}$, the expression of M-$\beta_{3\text{-}5}$-$GFP_{1\text{-}10}$, but not the other individual domains, decreased the binding of SQSTM1 to PDPK1, indicating that the binding of the M-$\beta_{3\text{-}5}$ segment to PDPK1 interfered with the baseline interaction between SQSTM1 and PDPK1 (Fig. 3C).

We then investigated whether SQSTM1 was phosphorylated by PDPK1. The phosphorylation level of T138, but not other residues,

Fig. 1 | Coronavirus M protein is degraded by SQSTM1-dependent autophagy. **A** Immunoblotting and immunoprecipitation of the lysates of HEK293T cells cotransfected with Flag-SQSTM1 and the indicated vectors expressing GFP tagged-PEDV M (GFP-PEDV M), GFP tagged-SARS-CoV-2 M (GFP-SARS M), GFP tagged-IBV M (GFP-IBV M), or GFP tagged-PDCoV M (GFP-PDCoV M). GFP was used as a control. **B** Schematic diagram of full-length or truncated SARS-CoV-2 M (GFP-M) protein structures, including various M truncated mutants that lacked the N-terminal disordered region (GFP-MΔDR1), transmembrane domain (GFP-MΔTM), conserved domain and/or β-sheets 1-5 (GFP-MΔCDβ$_{1\text{-}5}$, GFP-MΔCD, GFP-MΔβ$_{1\text{-}2}$ or GFP-MΔβ$_{3\text{-}5}$; β$_1$ and β$_2$ are outer sheets; β$_3$ to β$_5$ are inner sheets), C-terminal β-sheets 6-8 (GFP-MΔβ$_{6\text{-}8}$, GFP-MΔβ$_{6\text{-}7}$, GFP-MΔβ$_8$; β$_6$ and β$_7$ are outer sheets; β$_8$ is an inner sheet), and C-terminal disordered region (GFP-MΔDR2). **C** Immunoblotting and immunoprecipitation of the lysates of HEK293T cells cotransfected with Flag-SQSTM1 and the indicated vectors expressing full-length M (GFP-M) or various M truncated mutants (GFP-MΔDR1, GFP-MΔTM, GFP-MΔCDβ$_{1\text{-}5}$, GFP-MΔCD, GFP-MΔβ$_{1\text{-}2}$, GFP-MΔβ$_{3\text{-}5}$, GFP-MΔβ$_{6\text{-}8}$, GFP-MΔβ$_{6\text{-}7}$, GFP-MΔβ$_8$, GFP-MΔDR2). GFP was used as a control. **D** Schematic diagram of split GFP$_{1\text{-}10/11}$ fluorescence. When proteins fused with GFP$_{1\text{-}10}$ or GFP$_{11}$ interact, GFP$_{1\text{-}10}$ self-associate with GFP$_{11}$ to reconstitute a functional GFP. **E** Split GFP$_{1\text{-}10/11}$ florescence of the proteins between full length or mutant M fused with GFP$_{1\text{-}10}$ and SQSTM1 fused with GFP$_{11}$. **F** Quantification of split GFP$_{1\text{-}10/11}$ fluorescence. The split GFP$_{1\text{-}10/11}$ signal from (**E**) was calculated using ImageJ software. $n = 6$ images analyzed for each condition. **G** MST analysis of the indicated protein interactions. K_D measurements of SQSTM1 with different ligands (M, M-CD and MΔCD) were derived from the binding response as a function of the GFP-SQSTM1 concentration. **H** Immunoblotting of the lysates of HEK293T cells or *SQSTM1*-KO cells transefected with indicated vectors ($n = 3$ biological replicates). **I** Confocal analysis of colocalization between full length or mutant M and LC3B in presence or absence of SQSTM1. Statistical analysis was performed using unpaired two-tailed Student's *t*-tests, mean ± SEMs, $^*P < 0.05$, $^{**}P < 0.01$, $^{***}P < 0.001$, $^{****}P < 0.0001$. NS = *P* not significant. Source data are provided as a Source Data file.

gradually increased as the PDPK1 expression level increased (Fig. S3J). The PDPK1 inhibitor OSU-03012 blocked the phosphorylation of SQSTM1 at T138 in a dose-dependent manner (Fig. 3F). These results confirmed the role of PDPK1 in SQSTM1 phosphorylation.

An in vitro phosphorylation assay was performed to verify whether PDPK1 phosphorylated SQSTM1 directly. Prokaryotically expressed and purified GST-SQSTM1 or GST-SQSTM1-T138A was incubated with lysates of cells expressing Flag-PDPK1, Flag-PDPK1 S241A (phosphorylation-deficient mutant) or Flag-PDPK1 S241D (phosphorylation-mimic mutant) in the presence or absence of ATP (Fig. 3G). PDPK1 and S241D, but not S241A, were able to phosphorylate GST-SQSTM1 at T138 but not its T138A mutant in the presence of ATP, suggesting that PDPK1 directly phosphorylated SQSTM1 at T138 (Fig. 3G).

OSU-03012 inhibited M/PM-induced phosphorylation of SQSTM1 at T138 (Fig. 3H, I). M lacking either β$_{3\text{-}5}$ or the CD lost the ability to promote SQSTM1 phosphorylation (Fig. 3J). The above data indicated that M-β$_{3\text{-}5}$ or M-CD was required for M-mediated phosphorylation. Moreover, M expression and PEDV infection resulted in increased phosphorylation at the T138 site of SQSTM1 through the S241 site of PDPK1 (Figs. 3K and S3K-S3M).

Overall, the M protein promoted the phosphorylation of SQSTM1 at T138 by PDPK1.

Phosphorylation at T138 promotes the redirection of SQSTM1 from the M protein to the mitochondria to increase its degradation

We next wondered whether phosphorylation at T138 affected the interaction between SQSTM1 and the M protein or mitochondria. Anti-Flag IP revealed that T138A (a phosphorylation-deficient mutant) had a greater affinity for M than did the WT and T138D constructs, whereas T138D (a phosphorylation-mimic mutant) interacted with TOMM22 more strongly than did the WT and T138A constructs (Fig. 4A). Similarly, confocal microscopy analysis revealed that T138A and T138D significantly colocalized with M or mitochondria in cells, respectively (Fig. 4B). A dual split-fluorescence assay (Fig. 4C, D) revealed that in *SQSTM1*-KO cells, T138D increased the sfCherry2$_{1\text{-}10/11}$ signal, whereas T138A increased the GFP$_{1\text{-}10/11}$ signal and decreased the sfCherry2$_{1\text{-}10/11}$ signal. These results confirmed that T138 phosphorylation led to the transfer of SQSTM1 to mitochondria, whereas dephosphorylation resulted in its targeting of the M protein.

Next, a CHX chase assay showed that the expression of T138A increased the degradation of the M protein, whereas T138D expression decreased it (Fig. 4E). In contrast, TOMM22 degradation occurred more slowly after T138A expression but more quickly after T138D expression than after SQSTM1 expression (Fig. 4F). These results suggested that T138 phosphorylation inhibited M degradation but conversely promoted TOMM22 degradation. We next examined the role of the phosphorylation of SQSTM1 at T138 in mitophagy. Compared with EV or T138A construct expression, T138D mutant expression increased RFP fluorescence (Fig. S4A and S4B), indicating that T138 phosphorylation indeed promoted mitophagy.

In summary, the phosphorylation of SQSTM1 at T138 redirected SQSTM1 from the M protein to the mitochondria to promote its degradation (Fig. 4G).

The PDPK1-SQSTM1 axis is required for M-mediated mitophagy

We next investigated whether the M protein promotes mitophagy through the PDPK1-SQSTM1 axis. OSU-03012 treatment, *PDPK1* KO and *SQSTM1* KO reversed the effect of M on the shift in the green signal to a red signal, suggesting that M induced mitophagy through PDPK1 and SQSTM1 (Figs. 5A and S5A). Similarly, the expression of either PM or M decreased the levels of the mitochondrial outer membrane proteins MAVS and TOMM22 (Fig. 5B), whereas OSU-03012 restored the levels of these proteins, confirming that PDPK1 was needed for M-mediated mitophagy. Moreover, SQSTM1 knockout inhibited the reduction in MAVS and TOMM22 levels in the presence of M (Fig. 5C). Restoration of the expression of SQSTM1 or the T138D mutant, but not the T138A mutant, significantly rescued the degradation of MAVS and TOMM22 in the presence of M. These results confirmed that the phosphorylation of SQSTM1 at T138 was required for M-mediated mitophagy (Fig. 5C).

We next investigated the role of M-β$_{3\text{-}5}$ in M-induced mitophagy. M-β$_{3\text{-}5}$ inhibited the shift of the green signal to a red signal (Fig. S5A). Consistently, M-β$_{3\text{-}5}$ inhibited the M-mediated decrease in the levels of MAVS and TOMM22 (Fig. 5D). In addition, TEM analysis revealed that M expression resulted in the formation of several autophagic vesicles containing mitochondria, which were swollen and lacked their cristae ultrastructure (Fig. 5E). The expression of M-β$_{3\text{-}5}$ decreased the number of autophagosomes containing mitochondria and restored the number of mitochondria (Fig. 5F). The above data indicated that M-β$_{3\text{-}5}$ neutralized the ability of M to induce mitophagy.

We next investigated the effects of M or the β$_{3\text{-}5}$-lacking M mutant (MΔβ$_{3\text{-}5}$) on mitophagy during virus infection. The recombinant VSVs were constructed (Fig. 5G). VSV-M produced an obviously higher amounts of virus than did VSV-GFP or VSV-MΔβ$_{3\text{-}5}$ (Fig. S5B and S5C). Hematoxylin and eosin (H&E) staining of the lungs of the mice revealed that, in comparison with the VSV-GFP- or VSV-MΔβ$_{3\text{-}5}$-infected mice, the VSV-M-infected mice presented greater immune cell infiltration and more severe tissue damage (Fig. S5D). Infection with VSV-M, but not with VSV-GFP or VSV-MΔβ$_{3\text{-}5}$, led to a significant reduction in MAVS and TOMM22 expression, confirming that M induced mitophagy through the β$_{3\text{-}5}$ domain during virus replication (Fig. 5H).

In summary, M required the β$_{3\text{-}5}$ domain to promote mitophagy through the PDPK1-mediated phosphorylation of SQSTM1 at T138 (Fig. 5I).

https://doi.org/10.1038/s41467-024-53100-z

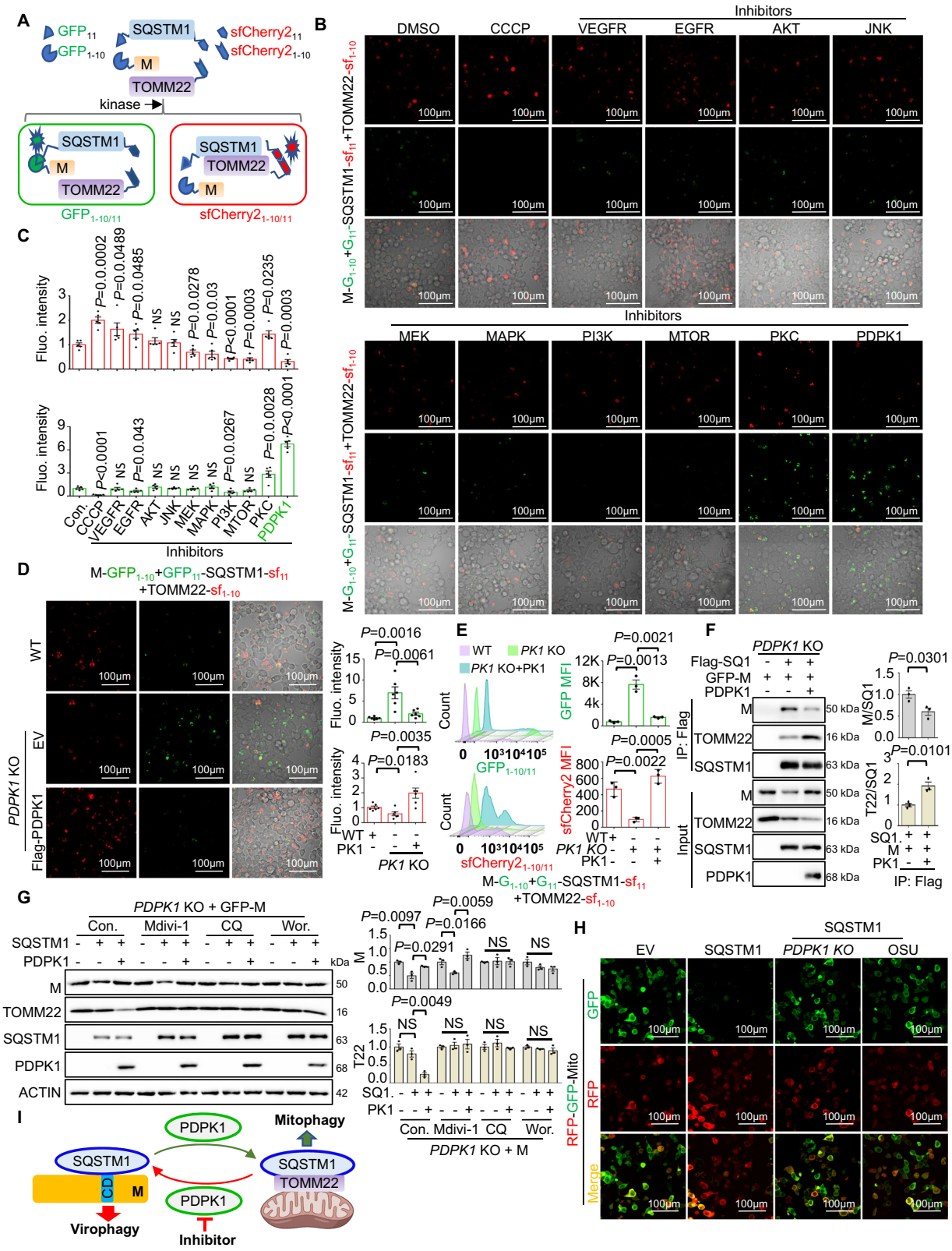

The PDPK1-SQSTM1 axis is required for M-mediated *IFNB1* inhibition

We next investigated whether M mediated *IFNB1* expression through PDPK1 and SQSTM1. A synthetic analog of double-stranded RNA (poly (I:C)) was used to stimulate the expression of *IFNB1* through RIGI/MDA5-MAVS in cells[22]. *IFNB1* messenger RNA (mRNA) expression was substantially increased in the presence of poly (I:C) ($P = 0.001$) but was significantly decreased upon M expression ($P = 0.0037$) (Fig. 6A). Knocking out either *SQSTM1* or *PDPK1* increased *IFNB1* expression in the context of poly (I:C) treatment and M expression (Fig. 6A), suggesting that M inhibited poly (I:C)-induced *IFNB1* expression through SQSTM1 and PDPK1.

In the presence of poly (I:C), M-$\beta_{3\text{-}5}$ reversed the M-mediated inhibition of *IFNB1* expression ($P = 0.0014$) but did not further increase

Fig. 2 | PDPK1 attenuates M degradation by redirecting SQSTM1 to mitochondria. A Schematic diagram of dual split-fluorescence for observing dynamic interactions between SQSTM1 fused with GFP_{11} and $sfCherry2_{11}$ and M fused with GFP_{1-10} or TOMM22 fused with $sfCherry2_{1-10}$. **B** Dual split-florescence of the indicated interactions between SQSTM1 and M (GFP_{1-10}) or TOMM22 ($sfCherry2_{1-10}$) in the presence of the indicated drugs. DMSO treatment was a control. **C** Quantification of dual split-florescence of the indicated interactions from (**B**). $n = 5$ images analyzed for each condition. **D**, **E** Confocal analysis and flow cytometry analysis (presented as fluorescence intensity and mean fluorescence intensity (MFI), respectively) of dual split-florescence of the interactions between M-GFP_{1-10} or TOMM22-sf_{1-10} and GFP_{11}-SQSTM1-sf_{11} in HEK293T or *PDPK1*-KO cells transfected with empty vector (EV) or Flag-PDPK1. $n = 6$ images analyzed for each condition in (**D**) and $n = 3$ biological replicates in (**E**). **F** Immunoblotting and anti-Flag immunoprecipitation of the lysates of *PDPK1*-KO HEK293T cells cotransefected with Flag-SQSTM1 and GFP-M, along with or without Myc-PDPK1 ($n = 3$ biological replicates). **G** Immunoblot analysis of the lysates of *PDPK1*-KO HEK293T cells transfected with the indicated vectors in the presence or absence of Mdivi-1, CQ or wortmannin (Wor.) ($n = 3$ biological replicates). **H** Confocal analysis of RFP-GFP-Mito upon SQSTM1 expression in presence or absence of knocking out of PDPK1 (*PDPK1* KO) or OSU-03012 (OSU) treatment. Empty vector (EV) was a vector control. **I** Schematic diagram of PDPK1 inhibiting the degradation of M. Created in BioRender. Hu, B. (2024) BioRender.com/m50x133. Statistical analysis was performed using unpaired two-tailed Student's *t*-tests, mean ± SEMs, $^{*}P < 0.05$, $^{**}P < 0.01$, $^{***}P < 0.001$, $^{****}P < 0.0001$. NS = *P* not significant. Source data are provided as a Source Data file.

IFNB1 expression in *SQSTM1*- or *PDPK1*-KO cells compared with that in WT cells (Fig. 6A). PEDV infection did not stimulate the IFN response, but the expression of PEDV M-β_{3-5} (PM-β_{3-5}) ($P = 0.0002$) or the knockout of *SQSTM1* ($P = 0.0023$) or *PDPK1* ($P = 0.0036$) increased *IFNB1* expression during PEDV infection (Fig. 6B). Moreover, PM-β_{3-5} expression did not further enhance the effect of knocking out *SQSTM1* or *PDPK1* on increasing *IFNB1* expression, confirming that M-β_{3-5} reversed the coronavirus-mediated inhibition of *IFNB1* expression through SQSTM1 and PDPK1 (Fig. 6B).

We next investigated whether the stable expression of M with or without β_{3-5} during virus infection affected *IFNB1* expression. Compared with VSV-GFP, VSV-M but not VSV-M$\Delta\beta_{3-5}$, inhibited the expression of *IFNB1* in 293 T cells ($P = 0.0044$) or in mice ($P = 0.0002$) (Fig. 6C, D). However, SQSTM1 and the T138D mutant, but not the T138A mutant, inhibited the *IFNB1* expression induced by VSV-M$\Delta\beta_{3-5}$, as well as that induced by poly (I:C) stimulation, in both WT and *PDPK1*-KO cells (Fig. 6C, E), suggesting that T138 phosphorylation was needed for the SQSTM1-mediated inhibition of *IFNB1* expression and that SQSTM1 functioned downstream of PDPK1. Consistently, OSU-03012 restored *IFNB1* expression during PEDV infection in cells or during VSV-M infection in cells and mice (Fig. 6F–H). *SQSTM1* knockout (*SQSTM1* KO) or *PDPK1* conditional knockout (*PDPK1* cKO) compromised the inhibitory effect of VSV-M on *IFNB1* expression ($P < 0.0001$), and OSU-03012 did not further increase *IFNB1* expression in *SQSTM1*-KO or *PDPK1*-cKO mice (Fig. 6G, H). These data suggested that M-β_{3-5} was needed for the M-mediated suppression of IFN production through the phosphorylation of SQSTM1 at T138 (Fig. 6I).

PDPK1 promotes viral replication through SQSTM1 in vitro and in vivo

We next found that the replication of PEDV was attenuated by OSU-03012 treatment and *PDPK1* KO but increased by PDPK1 overexpression (Fig. 7A–E).

The role of the phosphorylation of SQSTM1 at T138 in virus replication was then measured. The expression of SQSTM1 and T138D, but not T138A, restored the protein levels of PEDV M or VSV G (Fig. 7F, G). OSU-03012 treatment or *SQSTM1* knockout reduced PEDV M protein expression during PEDV infection, whereas OSU-03012 treatment did not further decrease the PEDV M protein level in *SQSTM1*-KO cells (Fig. 7H). The above data indicated that PDPK1-mediated T138 phosphorylation was required for the SQSTM1-mediated increase in virus replication.

We next elucidated the role of PDPK1 and SQSTM1 in the replication of viruses in mice. Knocking out *PDPK1* or *SQSTM1* or treating mice with OSU-03012 decreased the level of the VSV G protein, the viral titer and the viral load, resulting in reduced lung damage; however, treating *SQSTM1*-KO mice with OSU-03012 did not further decrease the level of the VSV G protein, the viral titer, or the viral load, indicating that PDPK1 promoted VSV-M replication through SQSTM1 (Fig. 7I–P).

In summary, PDPK1 promoted the replication of PEDV and VSV-M through SQSTM1.

Targeting PDPK1 with the interfering peptide Mβ_{3-5} inhibits viral replication by promoting virophagy and restoring *IFNB1* expression

We synthesized one interfering peptide and its corresponding scrambled peptide (SP) with a D-retroinverso (DRI) conformation based on the amino acid sequence of M-β_{3-5}, namely, IMβ_{3-5} and SP, to test the ability of IMβ_{3-5} to block virus replication by degrading M and inducing *IFNB1* expression (Fig. 8A).

IMβ_{3-5} prevented the PDPK1-mediated inhibition of the interactions between SQSTM1 and M, VP2, and PB1-F2 (Fig. 8B) and promoted the colocalization of GFP-LC3B with M, VP2, and PB1-F2 (Fig. 8C). Consistently, IMβ_{3-5} inhibited the phosphorylation of SQSTM1 at T138 by M (Fig. S6A) and promoted the degradation of M, VP2 and PB1-F2 even in the presence of PDPK1, and this degradation was blocked by CQ treatment (Fig. S6B–S6D). These data suggested that IMβ_{3-5} promoted the autophagic degradation of M, VP2 and PB1-F2 by blocking PDPK1. In addition, IMβ_{3-5} restored *IFNB1* expression in cells or in mice infected with VSV-M, IBDV or H1N1 (Fig. 8D–F).

We next found that, compared with the control, treatment with IMβ_{3-5} decreased the titers of VSV-M, PEDV, IBDV and H1N1 in cells and of VSV-M and H1N1 in mice (Figs. 8G–I, S6E and S6F), suggesting that IMβ_{3-5} significantly inhibited virus infection, attenuated inflammatory cell infiltration and lung damage, and increased the survival of virus-infected mice (Figs. 8J–O, and S6G-S6I).

Overall, IMβ_{3-5} inhibited the replication of VSV-M in vitro and in vivo by restoring virophagy and the mitochondria-mediated IFN response (Fig. 8P).

Discussion

ACRs are crucial for the selective degradation of both proviral and antiviral components during infection. However, the specific mediator regulating the ability of ACRs to distinguish between these components remains unidentified. SQSTM1, one of the most studied ACRs, has dual effects, with both beneficial and harmful effects on various diseases[23], including pathogen infection. Our study, which utilized a dual split-fluorescence assay, identified PDPK1 as a critical mediator of SQSTM1-dependent discrimination between the viral factor M and the antiviral factor mitochondria. PDPK1 facilitates viral replication by inhibiting virophagy and mitophagy-mediated interferon responses. Notably, a PDPK1-targeting peptide rescues interferon levels by inhibiting the autophagic degradation of antiviral components and enhancing virophagy, thereby amplifying antiviral effects. This model provides valuable insights into the dual role of autophagy in diseases and aids in the development of a framework for identifying key modulators that mediate the precise recognition of autophagy.

Selective autophagy acts as a double-edged sword in various disease contexts, highlighting the complexity of ACR regulatory mechanisms. ACRs can recognize and degrade both beneficial and

https://doi.org/10.1038/s41467-024-53100-z

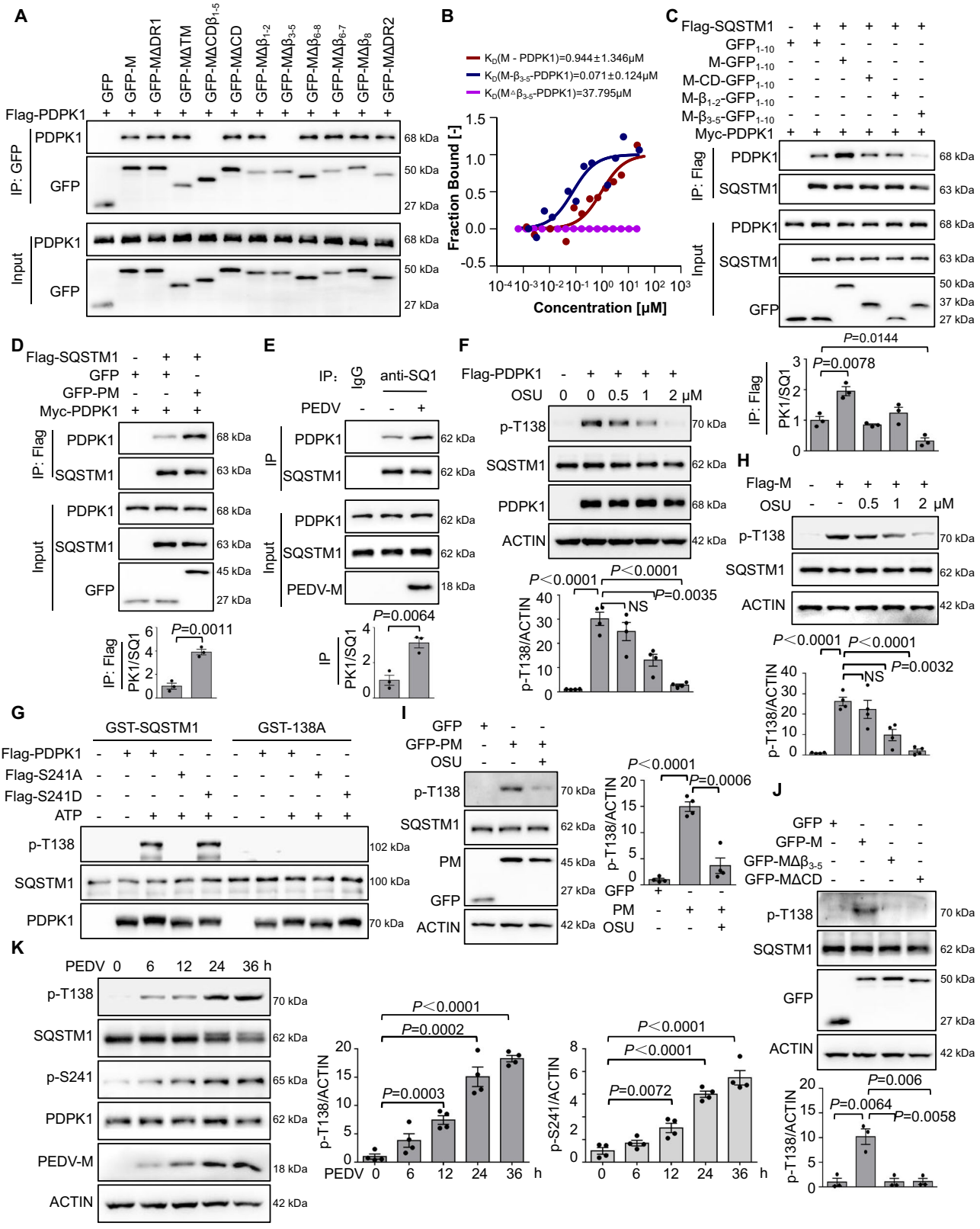

harmful substrates, leading to contrasting health effects depending on the context. In neurodegenerative diseases such as Alzheimer's disease and Parkinson's disease, ACRs such as SQSTM1 protect neurons by clearing toxic protein aggregates[24,25], but they can also mistakenly target healthy mitochondria, disrupting energy metabolism[26]. In cancer, autophagy can suppress tumorigenesis by degrading damaged mitochondria and preventing reactive oxygen species (ROS) accumulation[27]. However, tumors exploit autophagy to survive under stress by degrading tumor-suppressive factors[28]. In metabolic diseases such as diabetes and obesity, ACRs help maintain metabolic homeostasis by degrading excess lipid droplets and damaged mitochondria[29], but metabolic dysregulation can lead ACRs to mistakenly target essential enzymes, worsening the disease[30]. However, the key modulators that govern the precise recognition of substrates

Fig. 3 | PDPK1 directly phosphorylates T138 of SQSTM1. A Immunoblotting and immunoprecipitation of the lysates of HEK293T cells cotransfected with Flag-PDPK1 and the indicated vectors tagged with GFP expressing full-length M or various M truncated mutants (MΔDR1, MΔTM, MΔCDβ$_{1\text{-}5}$, MΔCD, MΔβ$_{1\text{-}2}$, MΔβ$_{3\text{-}5}$, MΔβ$_{6\text{-}8}$, MΔβ$_{6\text{-}7}$, MΔβ$_{8}$, MΔDR2). GFP was used as a control. **B** MST analysis of the indicated protein interactions. K_D measurements of PDPK1 with different ligands (M, M-β$_{3\text{-}5}$ and MΔβ$_{3\text{-}5}$) were derived from the binding response as a function of the GFP-PDPK1 concentration. **C** Immunoblotting and immunoprecipitation of the lysates of HEK293T cells cotransfected with Flag-SQSTM1 and Myc-PDPK1 in presence or absence of SARS-CoV-2 M (M) or its truncated mutants. GFP$_{1\text{-}10}$ was used as a control ($n = 3$ biological replicates). **D** Immunoblotting and immunoprecipitation of the lysates of HEK293T cells cotransfected with Flag-SQSTM1 and Myc-PDPK1 along with or without PEDV M (GFP-PM) ($n = 3$ biological replicates). **E** Immunoblotting and immunoprecipitation of the lysates of HEK293T cells in presence or absence of PEDV ($n = 3$ biological replicates). **F** Immunoblotting of phosphorylation of SQSTM1 at T138 of the lysates of HEK293T cells transfected with empty vector or Flag-PDPK1 in the presence or absence of OSU-03012 (OSU) ($n = 4$ biological replicates). **G** In vitro phosphorylation assay. The indicated proteins were incubated together in the presence or absence of ATP, and immunoblotting was performed. **H** Immunoblot analysis of phosphorylation of SQSTM1 at T138 of the lysates of HEK293T cells transfected with empty vector or SARS-CoV-2 M (Flag-M) in the presence or absence of different doses of OSU-03012 (OSU) ($n = 4$ biological replicates). **I** Immunoblot analysis of phosphorylation of SQSTM1 at T138 in HEK293T cells after overexpression of PEDV M (GFP-PM) in the presence or absence of OSU-03012 (OSU). GFP was used as a control ($n = 4$ biological replicates). **J** Immunoblot analysis of phosphorylation of SQSTM1 at T138 in HEK293T cells after overexpression of GFP, GFP-M, GFP-MΔβ$_{3\text{-}5}$ or GFP-MΔCD ($n = 4$ biological replicates). **K** Immunoblot analysis of phosphorylation of SQSTM1 at T138 and phosphorylation of PDPK1 at S241 in HEK293T cells as PEDV infection progressed ($n = 4$ biological replicates). Statistical analysis was performed using unpaired two-tailed Student's t-tests, mean ± SEMs, $^{*}P < 0.05$, $^{**}P < 0.01$, $^{***}P < 0.001$, $^{****}P < 0.0001$. NS = P not significant. Source data are provided as a Source Data file.

by ACRs, including both the pro- and anti-disease components mentioned above, remain unknown. The split-fluorescence assay screening model employed in our study may help provide a strategy to identify these modulators.

OSU-03012, a PDPK1 inhibitor, has broad-spectrum antiviral activity. A previous study revealed that OSU-03012 treatment rapidly reduces the levels of viral receptors, including NPC1 and TIM1 for Ebola/Marburg/Hepatitis A, LAMP1 for Lassa fever, NTCP1 for hepatitis B viruses, and ACE2 for SARS-CoV-2, as well as the spike protein of SARS-CoV-2, through autophagic degradation[31–36], suggesting that PDPK1 is a potential broad drug target for the treatment of various viruses by activating virophagy. Indeed, OSU-03012 inhibits the replication of viruses and extends animal survival[37]. Consistent with these findings, our study demonstrated that a PDPK1-targeting peptide significantly reduces the viral titer in mice infected with VSV-M and IAV. In conclusion, PDPK1 has emerged as a promising drug target for treating a broad spectrum of viral diseases through the activation of virophagy.

In vertebrates, the detection of actively replicating viruses relies primarily on the recognition of foreign RNA or DNA structures, which are traditionally referred to as pathogen-associated molecular patterns (PAMPs), by pathogen recognition receptors (PRRs). These PAMPs include a variety of conserved microbial molecular structures and products, in accordance with Janeway's theory of innate immunity[38]. Notably, our research revealed that a highly conserved motif, denoted "CD", within the M proteins of coronaviruses is a potential PAMP. We further identified SQSTM1 as a PRR that is responsible for the recognition of this motif. Furthermore, autophagy is critical for identifying CD, which would help minimize mistargeting due to viral variability and provide a promising direction for the development of new antiviral treatments, enabling cells to detect and respond efficiently to microbial threats.

Limitations of the study

Despite these insights, significant gaps remain in understanding ACRs and selective autophagy. Further elucidation of the molecular signals and posttranslational modifications regulating the substrate specificity of ACRs is crucial for developing targeted therapies that enhance beneficial autophagy while inhibiting detrimental processes. Additionally, the context-dependent nature of autophagy requires a deeper understanding of how different cellular environments and stress conditions affect ACR functions. Research should focus on these context-specific differences to tailor autophagy-based interventions. Moreover, the mechanisms by which pathogens subvert host autophagy need to be studied in detail to develop strategies that bolster host defenses. Designing drugs to precisely modulate ACR activity is a promising treatment avenue, potentially improving the outcomes of neurodegenerative diseases, cancer, and metabolic disorders. Addressing these gaps will unlock the full therapeutic potential of selective autophagy, transforming the prevention and treatment of a wide range of conditions and ultimately enhancing human health.

Our findings support the role of PDPK1 in inhibiting the specific recognition of viral components by SQSTM1, but the factors or post-translational modifications that promote the specific recognition of viral components by the ACR remain unknown. Additionally, our screen included only 20 autophagy-related kinase inhibitors. This scope could be expanded to include the entire genome in future research, aiming to identify additional specific mediators that distinguish between harmful and beneficial substrates in different disease contexts. These findings lay the foundation for targeted approaches to treat specific autophagy-related diseases.

Methods

Ethics statement

This study was approved by the Animal Ethical and Welfare Committee for Institutional Animal Care and Use Committee (IACUC) of Zhejiang University (approval no. ZJU20220495).

Materials and cell culture

HEK293T, Vero E6, DF-1 and MDCK cells were obtained from ATCC and cultured in Dulbecco's modified Eagle medium (DMEM) (Life Technologies, 12100-038) supplemented with 10% fetal bovine serum (Sigma Life Technologies, F2442). We used the following antibodies for our experiments: anti-phospho-PDPK1 rabbit mAb (Ser241) (#3061) and anti-phospho-Thr269/Ser272 SQSTM1 rabbit mAb (T269/S272) (#13121) from CST; anti-phospho-Ser403 (S403) SQSTM1 rabbit mAb (PA5-67516), anti-phospho-Ser28 SQSTM1 rabbit mAb (S28) (PA5-35409) and anti-phospho-Ser366 SQSTM1 rabbit mAb (S366) (PA5-105637) from Thermo Fisher; anti-phospho-T138 SQSTM1 rabbit mAb (T138) (ab285164), anti-SQSTM1 rabbit mAb (ab109012) and anti-FITC polyclonal antibody (71-1900) from Abcam; anti-MAVS (A5764), anti-TOMM22 (A14548) and anti-PDPK1 (A1665) rabbit mAbs from ABclonal; anti-FLAG (F1804) and anti-MYC (M5546) mouse mAbs from Sigma–Aldrich; and anti-ACTB/β-actin (R1207-1) rabbit from Hangzhou HuaAn Biotechnology. We used DAPI (10236276001) from Roche and the anti-HsPIK3C3 pAb (Z-R015) for immunoprecipitation from Echelon Biosciences, Inc. A DyLight 405-conjugated goat anti-mouse secondary antibody (A23110) was obtained from Abbkine. An Alexa Fluor™ 488-conjugated goat anti-mouse secondary antibody (A32723), Alexa Fluor™ 488-conjugated goat anti-rabbit secondary antibody (A32731), and Alexa Fluor™ 546 donkey anti-rabbit secondary antibody (A10040) were purchased from Invitrogen. The following specific labeled monoclonal antibodies were used for flow cytometry: BV421 rat anti-CD11b (M1/70) (562605), FITC rat anti-mouse Ly6G (1A8) (551460), PE-Cy7 Hamster anti-mouse CD11c (HL3) (558079), APC rat

https://doi.org/10.1038/s41467-024-53100-z

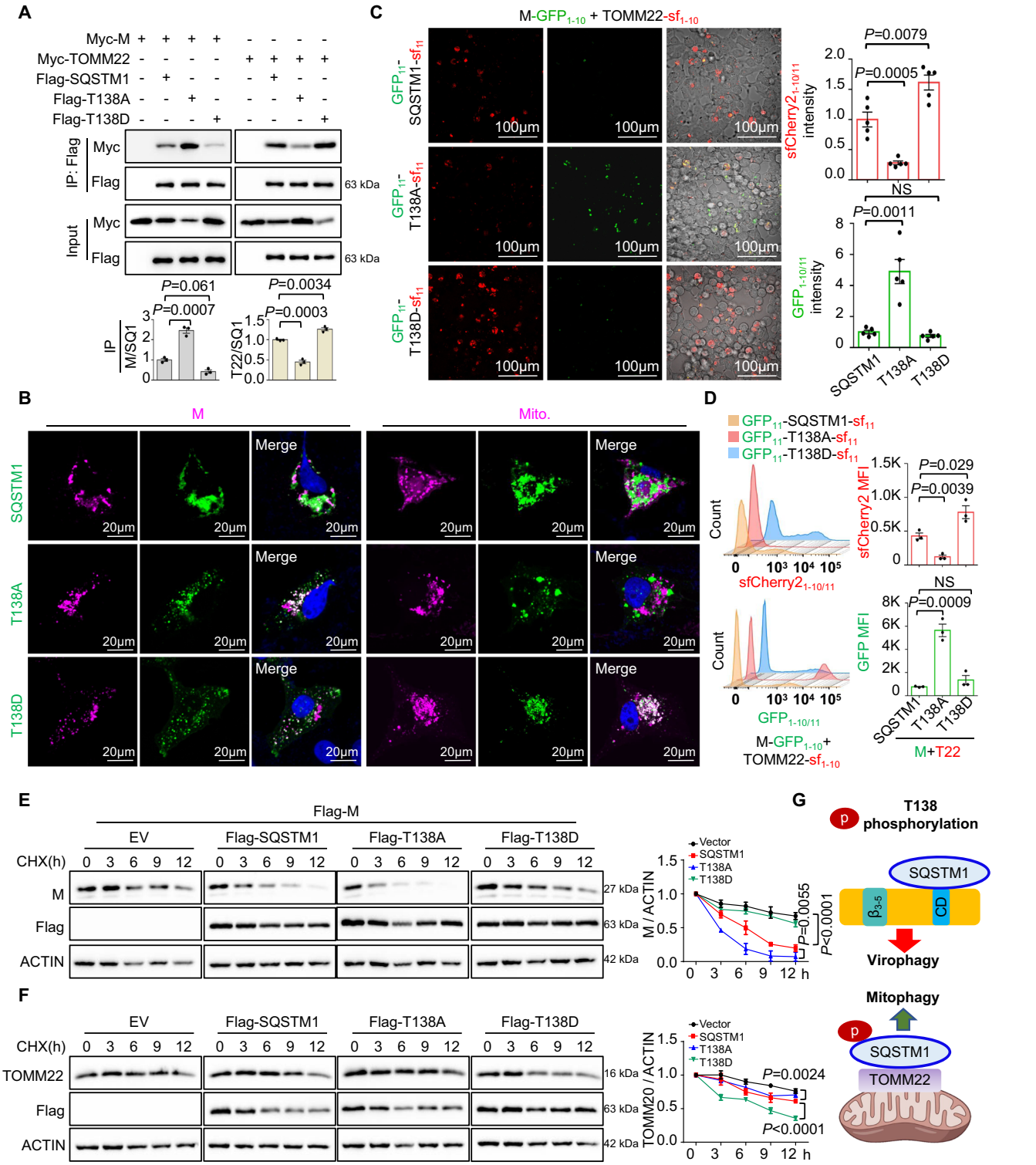

Fig. 4 | Phosphorylation at T138 promotes the redirection of SQSTM1 from the M protein to the mitochondria to increase its degradation. A Immunoblot analysis and anti-Flag immunoprecipitation of the lysates of *SQSTM1*-KO HEK293T cells cotransfected with Myc-SARS-CoV-2 M (Myc-M) or Myc-TOMM22 and empty vector, Flag-SQSTM1, Flag-SQSTM1-T138A (Flag-T138A) or Flag-SQSTM1-T138D (Flag-T138D) ($n = 3$ biological replicates). Statistical analysis was performed using unpaired two-tailed Student's t-tests. **B** Confocal analysis of the colocalization between GFP-M (M) or Mito-DsRed (Mito) and Flag-SQSTM1 (SQSMT1), Flag-SQSTM1-T138A (T138A) or Flag-SQSTM1-T138D (T138D). **C**, **D** Confocal analysis and flow cytometry analysis (presented as fluorescence intensity and mean fluorescence intensity (MFI), respectively) of dual split-fluorescence of the proteins between M-GFP_{1-10} or TOMM22-sf_{1-10} and GFP_{11}-SQSTM1-sf_{11}, GFP_{11}-T138A-sf_{11} or GFP_{11}-T138D-sf_{11} in *SQSTM1*-KO cell lines. $n = 5$ images analyzed for each condition in (**C**) and $n = 3$ biological replicates in (**D**). Statistical analysis was performed using unpaired two-tailed Student's t-tests. **E**, **F** Cycloheximide chase analysis of Flag-M or endogenous TOMM22 degradation upon expression of empty vector (EV), Flag-SQSTM1, Flag-SQSTM1-T138A (Flag-T138A) or Flag-SQSTM1-T138D (Flag-T138D) in *SQSTM1*-KO HEK293T cell lines ($n = 3$ biological replicates). Statistical analysis was performed using two-way Anova. **G** Schematic diagram of the effect of T138 phosphorylation of SQSTM1 on M or mitochondria. Created in BioRender. Hu, B. (2024) BioRender.com/m50x133. Data are presented as mean ± SEMs, $^{*}P < 0.05$, $^{**}P < 0.01$, $^{***}P < 0.001$, $^{****}P < 0.0001$. NS = *P* not significant. Source data are provided as a Source Data file.

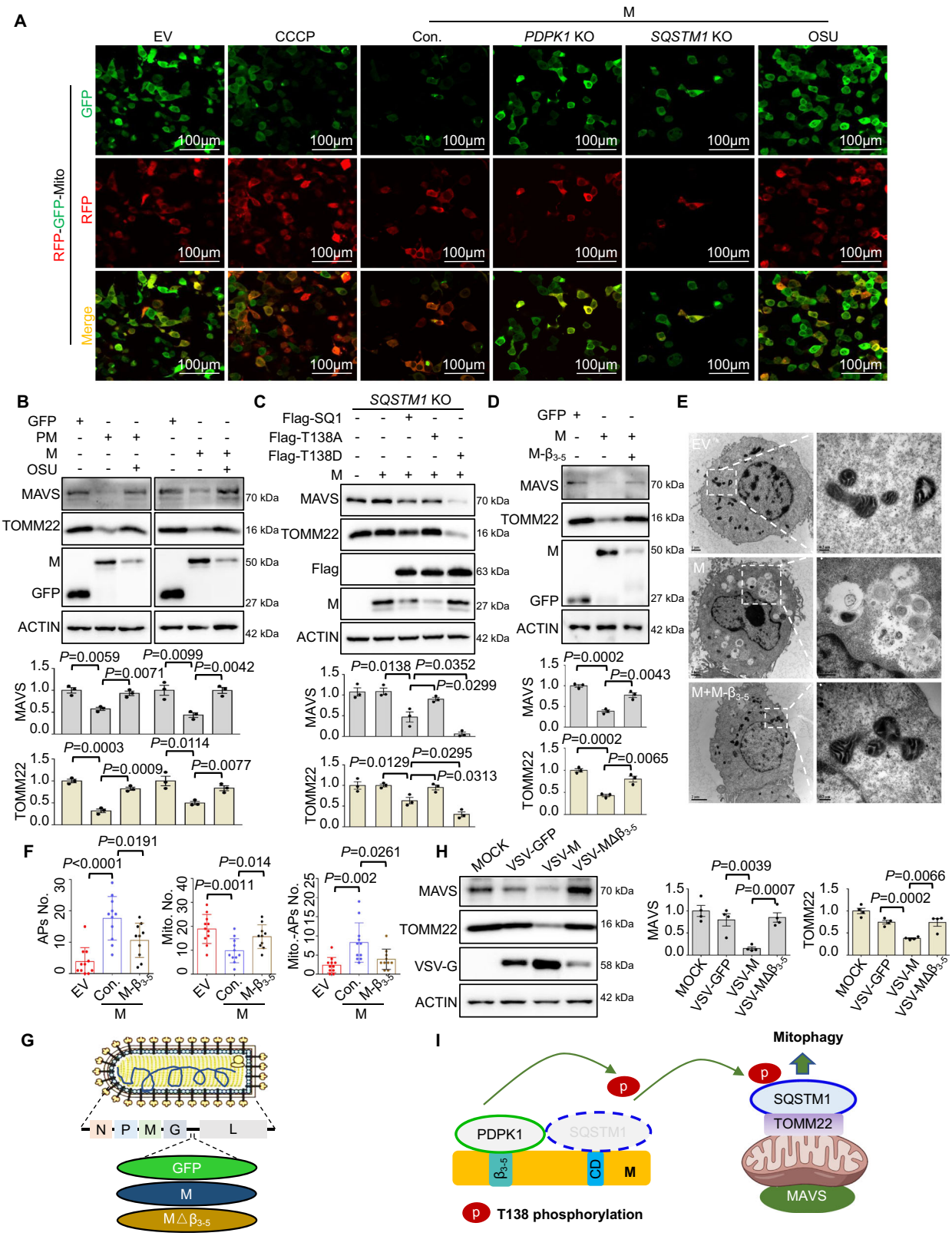

anti-mouse CD4 (RM4-5) (553051), BV510 rat anti-mouse I-A/I-E (M5/114) (742893) and PE rat anti-mouse F4/80 (T45-2342) (565410) from BD Pharmingen. Chemicals, including rapamycin (R8781), DMSO (472301), wortmannin (681676) and chloroquine phosphate (1118000), were purchased from Sigma–Aldrich. NP-40 lysis buffer (P0013F) was purchased from Beyotime. Protein A/G plus agarose (sc-2003) and anti-GFP mAb (sc9996) were obtained from Santa Cruz Biotechnology. ExFect™ transfection reagent (517051), TRIzol reagent (R401-01), a reverse transcription kit (R223-01) and AceQ Universal SYBR qPCR Master Mix (Q511-02) were purchased from Vazyme Biotech Co., Ltd. PMSF (P8340) and red blood cell lysis buffer (R1010) were purchased from Solarbio. CCCP (HY-100941), cycloheximide (CHX) (HY-12320), BAY 11-7082 (HY-13453), SCH772984 (HY-50846), staurosporine (HY-15141) and Mdivi-1 (HY-15886) were obtained from MedChemExpress. AZD4547 (SF5440), BIRB

Fig. 5 | The PDPK1-SQSTM1 axis is required for M-mediated mitophagy. **A** Confocal analysis of RFP-GFP-Mito upon expression of Flag-M (M) in WT, *PDPK1*-KO, and *SQSTM1*-KO HEK293T cell lines in the presence or absence of OSU-03012 (OSU). Empty vector (EV) transfection and CCCP treatment were used as the vector control and positive control, respectively. **B** Immunoblot analysis of mitochondrial proteins levels of cells upon expression of GFP, GFP-M (M) or GFP-PEDV M (PM) in the presence or absence of OSU-03012 (OSU) ($n = 3$ biological replicates). **C** Immunoblot analysis of mitochondrial proteins in *SQSTM1*-KO cells in presence or absence of Flag-M (M) upon expression of Flag-SQSTM1 (Flag-SQ1), Flag-SQSTM1-T138A (Flag-T138A) or Flag-SQSTM1-T138D (Flag-T138D) ($n = 3$ biological replicates). **D** Immunoblot analysis of mitochondrial proteins levels of cells upon expression of GFP or GFP-M in the presence or absence of GFP-tagged $\beta_{3\text{-}5}$ of M (GFP-M-$\beta_{3\text{-}5}$) ($n = 3$ biological replicates). **E** Transmission electron microscopy analysis of cells transfected with GFP-M (M) along with or without GFP-M-$\beta_{3\text{-}5}$ (M-$\beta_{3\text{-}5}$). Empty vector (EV) was used as a control. **F** Quantification of the number of autophagosomes (APs No.), mitochondria (Mito. No.) and autophagosomes containing mitochondria (Mito-APs No.) of the samples from (**E**). $n \geq 10$ cells analyzed for each condition. **G** Schematic of recombinant VSVs harboring GFP (VSV-GFP), M (VSV-M) or M$\Delta\beta_{3\text{-}5}$ (VSV-M$\Delta\beta_{3\text{-}5}$). Created in BioRender. Hu, B. (2024) BioRender.com/t28w795. **H** Immunoblot analysis of mitochondrial proteins in uninfected or VSV-GFP-, VSV-M-, and VSV-M$\Delta\beta_{3\text{-}5}$-infected cells ($n = 4$ biological replicates). **I** Schematic diagram showing that M promotes mitophagy through PDPK1 and SQSTM1. Created in BioRender. Hu, B. (2024) BioRender.com/m50x133. Statistical analysis was performed using unpaired two-tailed Student's *t*-tests, mean ± SEMs, $^{*}P < 0.05$, $^{**}P < 0.01$, $^{***}P < 0.001$, $^{****}P < 0.0001$. NS = *P* not significant. Source data are provided as a Source Data file.

796 (SD5928), GSK690693 (SF2789), SP600125 (S1876), trametinib (SD5973), tivozanib (SF5386), NVP-BEZ235 (SC0330), SB431542 (SF7890), OSU-03012 (SF2762), ruxolitinib (SD4740), erlotinib (SC0168), GW5074 (SD-5955), TAE226 (SC1076), Ro31-8220 (SC0344), AR-A014418 (SF2744), PP1 (SC1225) and collagenase type I (ST2294) were purchased from Beyotime Biotechnology. The capillaries (MO-K022) were obtained from Nanotemper Technologies.

Plasmid construction

The DNA sequences of SARS-CoV-2 M, IBV M and PDCoV M were synthesized by Sangon Biotech (Shanghai) Co., Ltd. The *PM* gene was amplified from the genome of the PEDV strain CV777. The IBDV *VP2* gene was cloned from the genome of the avibirnavirus IBDV strain NB. The *PB1-F2* gene of H1N1 was amplified from the genome of A/Puerto Rico/8/34 (PR8). The *SARS-CoV-2 M, IBV M, PDCoV M, PM, VP2 or PB1-F2* genes were subsequently inserted into the pEGFP-C3 (Clontech, 6082-1), pCMV-Flag-N (Clontech, 635688) or pCMV-Myc-N (Clontech, 635689) vector. SARS-CoV-2 M (M), IBDV VP2 and H1N1 PB1-F2 truncated variants were amplified from pEGFP-M, Flag-VP2 or pEGFP-PB1-F2 using specific primers. The primers used were as follows:

SARS-CoV-2 M△DR1-S: 5′-CGGACTCAGATCTCGAGGAAGAGCTTAAAAAGC-3′,

SARS-CoV-2 M△DR1-R: 5′-GCTTTTTAAGCTCTTCCTCGAGATCTGAGTCCG-3′;

SARS-CoV-2 M△TM-S: 5′-ACGGTACTATTACCGTTACGCGTTCCATGTGGTC-3′,

SARS-CoV-2 M△TM-R: 5′-GACCACATGGAACGCGTAACGGTAATAGTACCGT-3′;

SARS-CoV-2 M△CD$\beta_{1\text{-}5}$-S: 5′-CAGACTGTTTGCGCGTTGTGACATCAAGGACC-3′,

SARS-CoV-2 M△CD$\beta_{1\text{-}5}$-R: 5′-GGTCCTTGATGTCACAACGCGCAAACAGTCTG-3′;

SARS-CoV-2 M△CD-S: 5′-CAGACTGTTTGCGCGTATTCTTCTCAACGTGC-3′,

SARS-CoV-2 M△CD-R: 5′-GCACGTTGAGAAGAATACGCGCAAACAGTCTG-3′;

SARS-CoV-2 M△$\beta_{1\text{-}2}$-S: 5′-CAATCCAGAAACTAACCTAGAAAGTGAACTCG-3′,

SARS-CoV-2 M△$\beta_{1\text{-}2}$-R: 5′-CGAGTTCACTTTCTAGGTTAGTTTCTGGATTG-3′;

SARS-CoV-2 M△$\beta_{3\text{-}5}$-S: 5′-TGAACTCGTAATCGGATGTGACATCAAGGACC-3′,

SARS-CoV-2 M△$\beta_{3\text{-}5}$-R: 5′-GGTCCTTGATGTCACATCCGATTACGAGTTCA-3′;

SARS-CoV-2 M△$\beta_{6\text{-}8}$-S: 5′-TGACATCAAGGACCTGGGCAACTATAAATTAA-3′,

SARS-CoV-2 M△$\beta_{6\text{-}8}$-R: 5′-TTAATTTATAGTTGCCCAGGTCCTTGATGTCA-3′;

SARS-CoV-2 M△$\beta_{6\text{-}7}$-S: 5′-TGACATCAAGGACCTGGCTTCGCAGCGTGTAG-3′,

SARS-CoV-2 M△$\beta_{6\text{-}7}$-R: 5′-CTACACGCTGCGAAGCCAGGTCCTTGATGTCA-3′;

SARS-CoV-2 M△β_{8}-S: 5′-AGGTGACTCAGGTTTTGGCAACTATAAATTAA-3′,

SARS-CoV-2 M△β_{8}-R: 5′-TTAATTTATAGTTGCCAAAACCTGAGTCACCT-3′;

SARS-CoV-2 M△DR2-S: 5′-CAACTATAAATTAAACGAATTCGGCGGTAGCG-3′,

SARS-CoV-2 M△DR2-R: 5′-CGCTACCGCCGAATTCGTTTAATTTATAGTTG-3′;

IBDV VP2△PIR-S: 5′- CCATGGAG GCCCGAATTC GG ATGACAAACCTGCAAGAT-3′,

IBDV VP2△PIR -R: 5′- ATCCCCGCGGCCGCGGTACC TCACTCCATGAAGTACTCA-3′;

H1N1 PB1-F2△PIR -S: 5′- ACAGGAACAGGATACACCACAGAAGACAATGAACCAAG -3′,

H1N1 PB1-F2△PIR -R: 5′- CTTGGTTCATTGTCTTCTGTGGTGTATCCTGTTCCTGT -3′.

SQSTM1 (NM_003900.5), PDPK1 (NM_002613.5), and TOMM22 (NM_020243) were cloned from the HEK293T cell genome and inserted into pCMV-Flag-N or pCMV-Myc-N using specific primers. The primers 5′-TTGTACCCACATCTCCCCCCGCCGTTGTGA-3′ and 5′-TCACAACGGCGGGGGGAGATGTGGGTACAA-3′ were used to prepare Flag-SQSTM1△UBA, the SQSTM1 variant lacking UBA, with Flag-SQSTM1 serving as a template.

Cell transfection and treatment

For cell transfection, HEK293T or Vero E6 cells were seeded in the designated plates or on glass coverslips at a suitable density according to the experimental procedure. When the cells reached 70–80% confluence, they were transfected with ExFect™ Transfection Reagent, and immunoblotting or confocal microscopy was used to measure the protein levels or fluorescence signals.

For the experiments involving treatment with various kinase inhibitors, after transfection with GFP_{11}-SQSTM1-sf_{11} for 12 h, cell lines stably coexpressing TOMM22-$sf_{1\text{-}10}$ and M-$GFP_{1\text{-}10}$ were equally aliquoted onto 22 glass coverslips and cultured for another 12 h; then, they were treated with various kinase inhibitors at the following concentrations for 8 h: CCCP (10 μM), a well-known mitochondrial oxidative phosphorylation uncoupler that induces the opening of the permeability transition pore on the mitochondrial membrane, leading to the dissipation of mitochondrial membrane potential (Δψm); tivozanib (5 μM), a potent and selective VEGFR-1, -2 and-3 receptor inhibitor; erlotinib (5 μM), an EGF receptor tyrosine kinase inhibitor that selectively and reversibly inhibits the tyrosine kinase activity of EGFR; SB431542 (5 μM) is a selective and potent inhibitor of the TGF-β/Activin/NODAL pathway that inhibits ALK5, ALK4, and ALK7 by competing for the ATP binding site; GSK690693 (0.5 μM), a potent and selective, ATP-competitive, pan-AKT kinase inhibitor; trametinib (100 nM), a reversible and highly selective allosteric inhibitor of MEK1 and MEK2;

https://doi.org/10.1038/s41467-024-53100-z

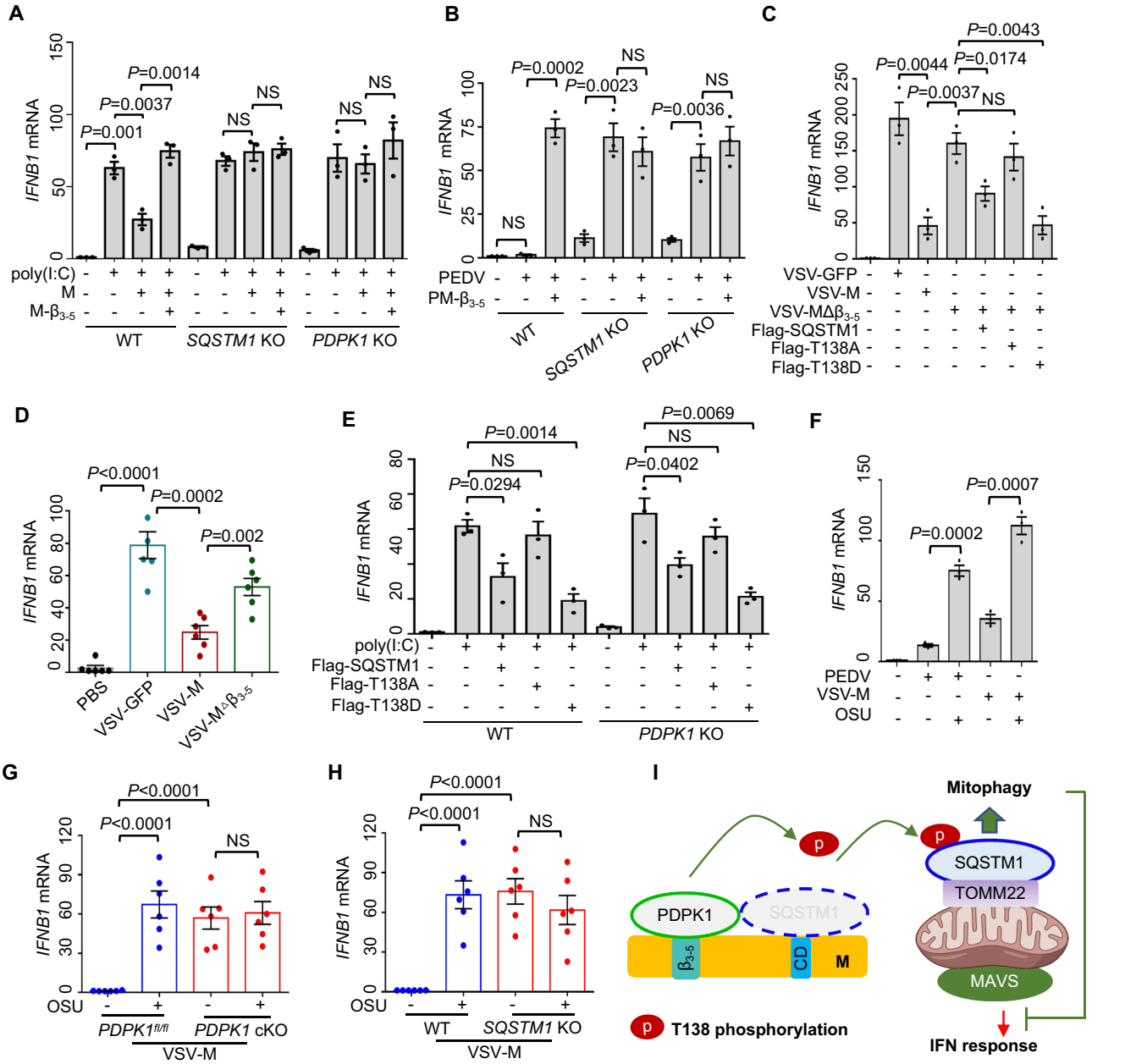

Fig. 6 | The PDPK1-SQSTM1 axis is required for M-mediated *IFNB1* inhibition. **A** Relative quantitation analysis of *IFNB1* mRNA expression in WT, *SQSTM1*-KO or *PDPK1*-KO HEK293T cells upon expression of M or M-$\beta_{3\text{-}5}$ in the presence or absence of poly (I:C) treatment ($n = 3$ biological replicates). **B** Relative quantitation analysis of *IFNB1* mRNA expression in WT, *SQSTM1*-KO or *PDPK1*-KO HEK293T cells upon expression of PM-$\beta_{3\text{-}5}$ in presence or absence of PEDV infection ($n = 3$ biological replicates). **C** Relative quantitation analysis of *IFNB1* mRNA expression in cells upon infection with VSV-GFP, VSV-M or VSV-M$\Delta\beta_{3\text{-}5}$ together with or without the expression of Flag-SQSTM1, Flag-SQSTM1-T138A (Flag-T138A), or Flag-SQSTM1-T138D (Flag-T138D) ($n = 3$ biological replicates). **D** Relative quantitation analysis of *IFNB1* mRNA expression in the lungs of mice (n = 6 mice/group) infected with VSV-GFP, VSV-M, or VSV-M$\Delta\beta_{3\text{-}5}$. PBS was used as a control. **E** Relative quantitation analysis of *IFNB1* mRNA expression in WT or *PDPK1*-KO 293T cells upon expression of Flag-SQSTM1, Flag-SQSTM1-T138A (Flag-T138A), and Flag-SQSTM1-T138D (Flag-T138D) in the presence or absence of poly (I:C) ($n = 3$ biological replicates). **F** Relative quantitation analysis of *IFNB1* mRNA expression in 293T cells infected with PEDV or VSV-M in the presence or absence of OSU-03012 (OSU) ($n = 3$ biological replicates). **G** Relative quantitation analysis of *IFNB1* mRNA expression in *PDPK1*$^{fl/fl}$ or *PDPK1*-cKO mice (n = 6 mice/group) infected with VSV-M in the presence or absence of OSU-03012 (OSU). **H** Relative quantitation analysis of *IFNB1* mRNA expression in WT or *SQSTM1*-KO mice (n = 6 mice/group) infected with VSV-M in the presence or absence of OSU-03012 (OSU). **I** Schematic diagram of M inhibiting IFN production through the PDPK1 and SQSTM1 axis. Created in BioRender. Hu, B. (2024) BioRender.com/m50x133. Statistical analysis was performed using unpaired two-tailed Student's *t*-tests, mean ± SEMs, $^{*}P < 0.05$, $^{**}P < 0.01$, $^{***}P < 0.001$, $^{****}P < 0.0001$. NS = *P* not significant. Source data are provided as a Source Data file.

BIRB 796 (10 μM), a high affinity and selective p38 MAPK inhibitor; NVP-BEZ235 (1 μM), an orally active and dual pan-class I PI3K and mTOR kinase inhibitor; rapamycin (5 μM), a potent and specific mTOR inhibitor; Ro 31-8220 (1 μM), a potent pan-PKC inhibitor; OSU-03012 (2 μM), a potent recombinant PDPK1 inhibitor; PP1 (1 μM), a reversible inhibitor of the SRC family of tyrosine kinases; GW5074 (2 μM), a potent and selective c-Raf inhibitor; SP600125 (10 μM), an orally active, reversible, and ATP-competitive JNK inhibitor; TAE226 (5 μM), a potent and ATP-competitive dual FAK and IGF-1R inhibitor; AR-A014418 (5 μM), a potent, selective and ATP-competitive GSK3β inhibitor;

https://doi.org/10.1038/s41467-024-53100-z

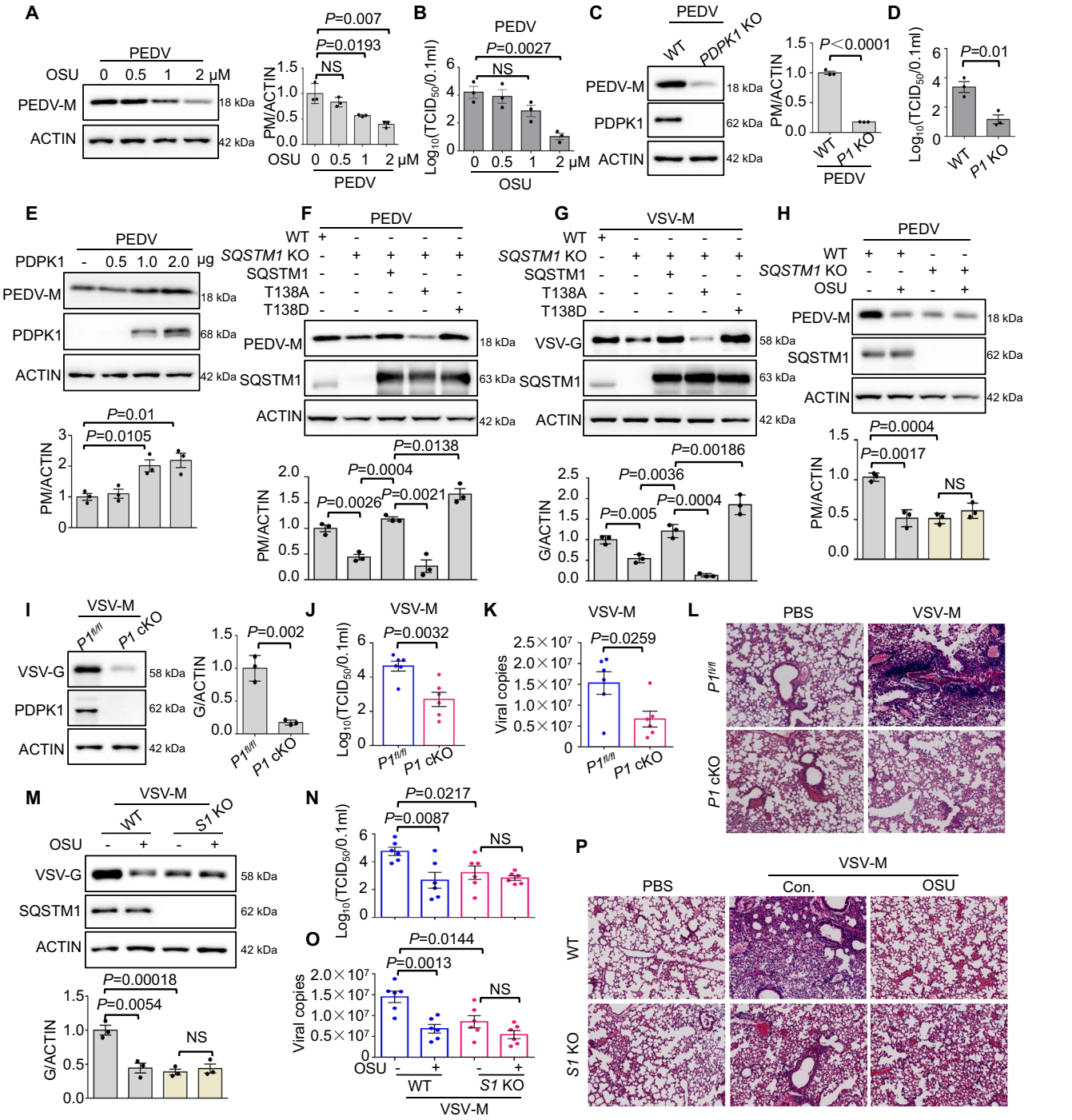

AZD4547 (10 μM), a potent inhibitor of the FGFR family; BAY 11-7082 (10 μM), an IκBα phosphorylation and NF-κB inhibitor; Ruxolitinib (100 nM), a potent and selective JAK1/2 inhibitor; SCH772984 (1 μM) a highly selective and ATP-competitive ERK inhibitor; and staurosporine (100 nM), a potent, ATP-competitive and non-selective inhibitor of protein kinases. DMSO was used as a control. The live cells were observed via confocal microscopy.

For the experiments involving treatment with autophagy inhibitors, after transfection with the indicated vectors for 24 h, the cells were treated with DMSO, Mdivi-1 (2.5 μM), CQ (50 μM), or wortmannin (Wor., 5 μM) for 4 h. The cells were then collected for subsequent analysis by immunoblotting.

For the CHX chase assay, 24 h after transfection, the cells were treated with 100 ng/ml CHX dissolved in DMSO. The cells were then harvested at various time points. Finally, the samples were subjected to immunoblot analysis. ImageJ software and GraphPad software were used to analyze the protein levels.

Cell viability

The viability of HEK293T and Vero E6 cells was measured with the colorimetric 3-(4,5-dimethylthiazol-2-yl)-2,5-diphenyltetrazolium bromide (MTT) test (Beyotime, C0009S). HEK293T or Vero E6 cells were seeded in 100 μl of medium in each well of 96-well plates and cultured for 24 h at 37 °C. The medium was then changed to fresh medium, and the cells were exposed to OSU-03012 at different concentrations ranging from 0 to 20 μM for 8 h. After the incubation period, 10 μl of MTT reagent was added to each well, and the cells were incubated at 37 °C for 4 h until the formazan had completely dissolved. The absorbance

Fig. 7 | PDPK1 promotes viral replication through SQSTM1 in vitro and in vivo. **A** Immunoblot analysis of PEDV M protein in HEK293T cells infected with PEDV (MOI = 0.001) upon OSU-03012 (OSU) treatment at different doses ($n = 3$ biological replicates). **B** Viral $TCID_{50}$ of samples of cells infected with PEDV (MOI = 0.001) upon OSU-03012 (OSU) treatment ($n = 3$ biological replicates). **C** Immunoblot analysis of PEDV M protein in WT and *PDPK1*-KO (*P1* KO) cells infected with PEDV using the indicated antibodies ($n = 3$ biological replicates). **D** $TCID_{50}$ of virus from WT and *PDPK1*-KO (*P1* KO) cells infected with PEDV ($n = 3$ biological replicates). **E** Immunoblot analysis of PEDV M protein in cells infected with PEDV upon expression of Flag-PDPK1 ($n = 3$ biological replicates). **F**, **G** Immunoblot analysis of the lysate in PEDV- or VSV-M- infected WT or *SQSTM1*-KO cells with or without expression of Flag-SQSTM1 (SQSTM1), Flag-SQSTM1-T138A (T138A) and Flag-SQSTM1-T138D (T138D) ($n = 3$ biological replicates). **H** Immunoblot analysis of PEDV M protein in WT or *SQSTM1*-KO cells infected with PEDV in the presence or absence of OSU-03012 (OSU) ($n = 3$ biological replicates). **I** Immunoblot analysis of VSV G protein in lung from $PDPK1^{fl/fl}$ ($P1^{fl/fl}$) and *PDPK1*-cKO (*P1* cKO) mice (n = 3 mice/group) infected with VSV-M (5×10^8 p.f.u. per mouse). **J** Viral $TCID_{50}$ of lungs from $PDPK1^{fl/fl}$ ($P1^{fl/fl}$) and *PDPK1*-cKO (*P1* cKO) mice (n = 6 mice/group) infected with VSV-M was measured. **K** The viral copies in lung tissues from $PDPK1^{fl/fl}$ ($P1^{fl/fl}$) and *PDPK1*-cKO (*P1* cKO) mice (n = 6 mice/group) infected with VSV-M were calculated using absolute quantification RT-qPCR. **L** Histopathology of lung sections from $PDPK1^{fl/fl}$ ($P1^{fl/fl}$) and *PDPK1*-cKO (*P1* cKO) mice infected with or without VSV-M. **M** Immunoblot analysis of the lungs from WT and *SQSTM1*-KO (*S1* KO) mice (n = 3 mice/group) infected with VSV-M (5×10^8 p.f.u. per mouse) in the presence of Cremophor (control) or OSU-03012 (OSU). **N** Viral $TCID_{50}$ in lungs from WT and *SQSTM1*-KO (*S1* KO) mice (n = 6 mice/group) infected with VSV-M in the presence of Cremophor (control) or OSU-03012 (OSU) were measured. **O** Viral copies in lungs from WT and *SQSTM1*-KO (*S1* KO) mice (n = 6 mice/group) infected with VSV-M in the presence of Cremophor (control) or OSU-03012 (OSU) were measured by absolute quantification RT-qPCR. **P** Histopathology of lung sections from WT and SQSTM1-KO (*S1* KO) mice uninfected or infected with VSV-M in the presence or absence of OSU-03012 (OSU). PBS was a negative control. Statistical analysis was performed using unpaired two-tailed Student's *t*-tests, mean ± SEMs, $^*P < 0.05$, $^{**}P < 0.01$, $^{***}P < 0.001$, $^{****}P < 0.0001$. NS = *P* not significant. Source data are provided as a Source Data file.

was measured within an hour using a multiplate reader with a test wavelength of 570 nm.

Virus propagation

PEDV, IBDV or H1N1 was propagated in Vero E6, DF-1 or MDCK cells, respectively. Vesicular stomatitis virus (VSV) was generated in HEK293T cells. Recombinant VSV strains harboring GFP, M or $M\Delta\beta_{3\text{-}5}$ were constructed by inserting the coding sequences of GFP, M and $M\Delta\beta_{3\text{-}5}$ into the VSV backbone between the VSV glycoprotein (G protein) and polymerase protein (L protein) at the NheI and XhoI restriction enzyme sites, and a vesicular stomatitis virus (VSV) with attenuated virulence was generated from the original strain by introducing the M51R substitution into the matrix gene[39]. The recombinant VSV-GFP, VSV-M or VSV-$M\Delta\beta_{3\text{-}5}$ was subsequently recovered in Vero E6 cells.

Construction of 293T cell lines stably expressing two genes

The TOMM22-$sf_{1\text{-}10}$ and M-$GFP_{1\text{-}10}$ genes were cloned and inserted into the lentiviral vector pCDH-CMV-MCS-EF1-Puro (System Biosciences, CD510B-1). The two constructs were subsequently cotransfected with ViraPower Lentiviral Packaging Mix (psPAX2; Addgene, 12260) and pMD2.G (Addgene, 12259) into HEK293T cells for 48 h at a 4:3:1 ratio, with an empty vector serving as a control. The cell supernatants containing viral particles were harvested and used to infect 293 T cells. At 24 h after infection, the cells were passaged and selected with 10 μg/ml puromycin. The expression of the above genes in the 293 T cell line was validated by immunoblot analysis.

Immunoblot analysis

Equal amounts of total protein from different samples were separated by SDS–PAGE, and the proteins were transferred to nitrocellulose blotting membranes (GE Healthcare Life Sciences, 10600001). After being blocked with 5% nonfat dry milk containing 0.1% Tween 20 (Sigma–Aldrich, P1379-500ML) for 30 min at 37 °C, the membranes were incubated with primary antibodies for 2 h at 37 °C, followed by an incubation with horseradish peroxidase-conjugated anti-mouse/rabbit IgG (Kirkegaard & Perry Laboratories, Inc., 074-1506) and visualization using a SuperSignal West Femto Substrate Trial Kit (Thermo Scientific/Pierce, 34095). The amounts of proteins were analyzed by FIJI (v 2.3.0). The uncropped and unprocessed scans of the blots were provided in the Source Data file

Immunofluorescence staining

The cells were plated in 35-mm glass-bottom cell culture dishes at a density of 6×10^4 cells/ml. Within 24 h, the cells were transfected with the indicated plasmids and treated with the indicated drugs or cultured in starvation medium. After 24 h or 48 h, the cells were fixed with 4% paraformaldehyde in PBS for 10 min at room temperature and then blocked with 5% nonfat milk for 1 h. After three washes with PBST (137 mM NaCl [Sinopharm Chemical Reagent Co., Ltd., 10019318], 2.7 mM KCl [Sinopharm Chemical Reagent Co., Ltd., 10016318], 10 mM Na_2HPO_4 [Sinopharm Chemical Reagent Co., Ltd., 10020318], 1.8 mM KH_2PO_4 [Sinopharm Chemical Reagent Co., Ltd., 10017618], and 0.1% Tween 20 [Sigma–Aldrich, P1379-500ML], pH 7.4], the cells were incubated with the indicated primary antibodies for 2 h at 37 °C. Then cells were washed with PBST and then incubated with secondary antibodies conjugated with DyLight 405 (Abbkine, A23110), Alexa Fluor 488 (Invitrogen, A32723 and A32731) or Alexa Fluor 546 (Invitrogen, A10040) for 1 h at 37 °C. Finally, the cells were observed under a Nikon A1R/A1 laser-scanning confocal microscope (Nikon).

Co-IP assay

The cell lines were separately cotransfected with the indicated recombinant vectors and then lysed with NP-40 lysis buffer. The cell lysates were incubated with an anti-FLAG antibody or an anti-GFP antibody and Protein A/G beads for 4 h at 4 °C. After centrifugation, the supernatants were removed, and the pellets were resuspended in washing buffer. The centrifugation and resuspension of the pellets in fresh washing buffer were performed five times. Finally, the pellets were lysed in lysis buffer for immunoblot analyses.

Affinity isolation assay

For GST affinity isolation, M, PDPK1 and TOMM22 were cloned and inserted into the pET-28A plasmid (Novagen, 69864). SQSTM1, M and M-$\beta_{3\text{-}5}$ were separately cloned and inserted into the pGEX4T-1 plasmid (Merck, GE28-9545-49). These constructs were subsequently transformed into *E. coli* BL21 cells for expression. His-PDPK1, His-M and His-TOMM20 were purified using Ni-NTA (QIAGEN, 30230). GST-SQSTM1, GST-M, and GST-M-$\beta_{3\text{-}5}$ were purified using Pierce™ glutathione agarose (Thermo Fisher Scientific, 16100) and washed with 1 ml of cold 1× PBS per 10 mg of reduced glutathione. Purified GST and GST fusion proteins were immobilized on glutathione agarose beads to prepare the bait proteins, and His-PDPK1, His-M or His-TOMM20 was used as the prey protein. A total of 0.1 mg of bait protein was added to the corresponding prey protein, which was incubated for 4 h at 4 °C, washed with NP-40 lysis buffer and then boiled in sample buffer. Finally, the samples were separated on 12% SDS–PAGE gels and immunoblotted with a mouse anti-His mAb (Huaan Biological Technology, M0812-3) and a mouse anti-GST mAb (Huaan Biological Technology, EM80701).

https://doi.org/10.1038/s41467-024-53100-z

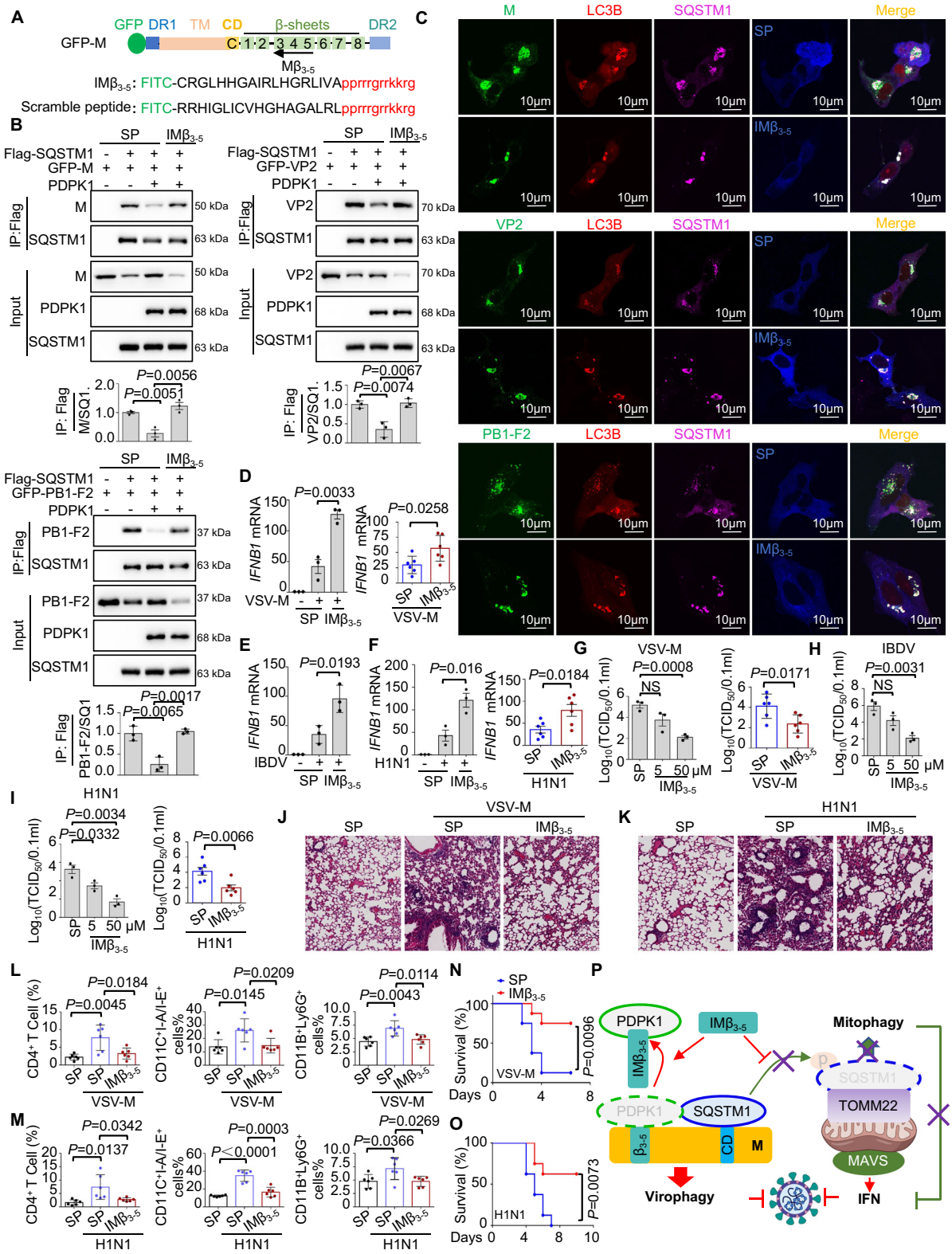

In vitro phosphorylation assay

HEK293T cells were transfected with the empty vector, Flag-PDPK1, Flag-PDPK1-S241A (Flag-S241A), or Flag-PDPK1-S241D (Flag-S241D) and lysed with NP40 lysis buffer containing phenylmethylsulfonyl fluoride (1 mM) 24 h after transfection. Then, immunoprecipitation was performed using a magnetic bead-conjugated mouse anti-Flag mAb (ABclonal, AE037, 1:100 dilution). The precipitated proteins (20 μg) were incubated with GST-SQSTM1 or GST-SQSTM1-138A (GST-138A) purified from *E. coli* BL21 cells in kinase buffer [20 mM Tris-HCl (pH 7.5), 10 mM $MgCl_2$, and 1 mM DTT] in the presence or absence of 100 μM ATP for 30 min at 37 °C. The reaction was stopped by the addition of 2× SDS loading buffer, and the proteins were subjected to SDS–PAGE and immunoblotting as described above.

Fig. 8 | Targeting PDPK1 with the interfering peptide Mβ$_{3\text{-}5}$ inhibits viral replication by promoting virophagy and restoring *IFNB1* expression. **A** Schematic diagram of the interfering peptide (black) which was labeled with FITC (green) at N-terminus and linked with cell penetrating peptide (red) at C-terminus. The sequence of the interfering peptide was a reversed sequence of the parent peptide and made by D-amino acids. Scramble peptide (SP) derived from the parent peptide was used as control. **B** Immunoblotting and anti-Flag immunoprecipitation of the lysates of HEK293T cells cotransfected with Flag-SQSTM1 and GFP-M, IBDV VP2 (GFP-VP2) or H1N1 PB1-F2 (GFP-PB1-F2) with or without PDPK1 in the presence of SP or IMβ$_{3\text{-}5}$ ($n = 3$ biological replicates). **C** Confocal analysis of SQSTM1-mediated colocalization between M, VP2 or PB1-F2 and LC3B in the presence of SP or IMβ$_{3\text{-}5}$. **D** Relative quantitation analysis of *IFNB1* mRNA in VSV-M-infected cells ($n = 3$ biological replicates) or in lungs of VSV-M-infected mice (n = 6 mice/group) in the presence of SP or IMβ$_{3\text{-}5}$. **E** Relative quantitation analysis of *IFNB1* mRNA expression in IBDV-infected cells in the presence of SP or IMβ$_{3\text{-}5}$ ($n = 3$ biological replicates). **F** Relative quantitation analysis of *IFNB1* mRNA expression in H1N1-infected cells ($n = 3$ biological replicates) or mice (n = 6 mice/group) in the presence of SP or IMβ$_{3\text{-}5}$. **G** Viral TCID$_{50}$ in VSV-M-infected cells ($n = 3$ biological replicates) or lungs from mice (n = 6 mice/group) in the presence of SP or IMβ$_{3\text{-}5}$ was calculated. **H** Viral TCID$_{50}$ in IBDV-infected cells in the presence of SP or IMβ$_{3\text{-}5}$ was calculated ($n = 3$ biological replicates). **I** The TCID$_{50}$ of virus in H1N1-infected cells ($n = 3$ biological replicates) or mice (n = 6 mice/group) in the presence of SP or IMβ$_{3\text{-}5}$ was measured. **J**, **K** Histopathology of lung sections from mice infected with or without VSV-M or H1N1 in presence or absence of SP or IMβ$_{3\text{-}5}$. **L**, **M** The proportion of CD4$^+$ T cells, CD11c$^+$I-A/I-E$^+$ dendritic cells and CD11b$^+$Ly6G$^+$ neutrophilic cells in the lungs of uninfected and VSV-M-or H1N1-infected mice (n = 6 mice/group) treated with SP or IMβ$_{3\text{-}5}$ were detected by flow cytometry. **N**, **O** Survival of VSV-M- or H1N1-infected mice treated with SP or IMβ$_{3\text{-}5}$ up to day 8 (n = 8 mice/group). **P** Schematic diagram of the inhibitory effect of IMβ$_{3\text{-}5}$ on viral replication. Created in BioRender. Hu, B. (2024) BioRender.com/t28w795. Statistical analysis was performed using unpaired two-tailed Student's *t*-tests, mean ± SEMs (**B**, **D-I**, **L**, **M**) or Log-rank test (**N**, **O**), $^*P < 0.05$, $^{**}P < 0.01$, $^{***}P < 0.001$, $^{****}P < 0.0001$. NS = *P* not significant. Source data are provided as a Source Data file.

Preparation of cell samples for mass-spectrometry

HEK293T cells transfected with Myc-SQSTM1 or cotransfected Myc-SQSTM1 and Flag-M were collected and lysed using NP40 lysis buffer (Beyotime, P0013F) supplemented with PMSF (Solarbio, P0100). Cellular lysates were incubated with mouse anti-Myc mAb for 4 h, followed by incubation with protein A/G beads (Santa Cruz Biotechnology, sc-2003) for 4 h at 4 °C. The samples were centrifuged and supernatants were removed. Then, the pellets were resuspended with NP40 as a wash buffer, repeated five times. Finally, the pellets were sent to company (Applied Protein Technology, China) for further analysis by mass-spectrometry.

Microscale thermophoresis assays

The affinity of GFP-SQSTM1 for M, M-CD and MΔCD or of GFP-PDPK1 for M, M-β$_{3\text{-}5}$ and MΔβ$_{3\text{-}5}$ was measured using the Monolith NT.115 system (NanoTemper Technologies). HEK293T cells were transfected with vectors expressing GFP-SQSTM1 or GFP-PDPK1 and lysed with NP40 lysis buffer containing phenylmethylsulfonyl fluoride (1 mM) at 36 h post-transfection. The cell lysates served as a target. Unlabeled M, M-CD, MΔCD, M-β$_{3\text{-}5}$ or MΔβ$_{3\text{-}5}$ was used as the ligand. For each assay, the target protein (~7.5 μM) was incubated with 16 different concentrations of unlabeled M, M-CD, MΔCD, M-β$_{3\text{-}5}$ or MΔβ$_{3\text{-}5}$ in the same volume of phosphate-buffered saline [PBS, 137 mM NaCl, 2.7 mM KCl, 10 mM Na_2HPO_4, and 1.8 mM KH_2PO_4, pH 7.4] supplemented with 0.02% Tween 20 at room temperature for 20 min. The samples were then loaded into capillaries (NanoTemper Technologies, MO-K022) and measured at 25 °C using 20–40% LED power and 20% MST power. Data were analyzed using Nanotemper analysis software MO. Affinity Analysis (v 2.3.0.).

RNA extraction and quantitative real-time PCR (RT–qPCR)

Total RNA from cell or mouse lung samples was extracted with TRIzol reagent according to the manufacturer's instructions, and the RNA was reverse transcribed into cDNA using a reverse transcription kit. Relative quantification RT-qPCR and absolute quantification RT-qPCR were performed on a Roche LC96 real-time PCR system using AceQ Universal SYBR qPCR Master Mix with specific primers. The sequences of the primers used were as follows:

mouse *IFNB1* S: 5′- TCCTGCTGTGCTTCTCCACCACA-3′,
mouse *IFNB1* R: 5′-AAGTCCGCCCTGTAGGTGAGGTT-3′;
mouse *GAPDH* S: 5′-GTCAAGGCCGAGAATGGGAA 3′,
mouse *GAPDH* R: 5′-CTCGTGGTTCACACCCATCA-3′;
human *IFNB1* S: 5′ -ACTGCAACCTTTCGAAGCCT-3′,
human *IFNB1* R: 5′ AAGTCCGCCCTGTAGGTGAGGTT 3′;
human *GAPDH* S: 5′ CGGGAAGCTTGTGATCAATGG 3′,
human *GAPDH* R: 5′ GGCAGTGATGGCATGGACTG 3′;

GAPDH was used as an internal control for normalization. The results were calculated using the $2^{-\Delta\Delta}$Ct method.

Virus infection and viral titer detection

HEK293T, Vero E6 or DF-1 cells were cultured in 12- or 24-well plates and infected with PEDV, recombinant VSVs, IBDV or H1N1, which were diluted in serum-free DMEM at a multiplicity of infection (MOI) of 0.001 or 0.01. After 1 h of absorption at 37 °C, the medium was removed. The infected cells were then washed with PBS three times and cultured in fresh DMEM supplemented with 2% FBS at 37 °C until the indicated time.

At different time points after infection, the cells were harvested and freeze–thawed three times. After centrifugation at 12,000 × *g* for 10 min at 4 °C, the supernatants were subjected to TCID$_{50}$ (50% tissue culture infective dose) detection. Briefly, the viral suspension was diluted 10-fold with DMEM supplemented with 2% FBS and subsequently added to fresh Vero E6, DF-1 or MDCK cells in 96-well plates. Eight replicates of each diluted sample were tested. At 48 h after infection, the cells were subjected to IFA with the indicated antibodies. Viral titers were determined by observing the infected cells under a fluorescence microscope (OLYMPUS, U-RFL-T), and the TCID$_{50}$ at 0.1 mL was calculated according to the Reed–Muench method.

Animals and mouse breeding

PDPK1$^{fl/fl}$ mice were kindly provided by Zhong-Zhou Yang (State Key Laboratory of Pharmaceutical Biotechnology, Department of Cardiology, Nanjing Drum Tower Hospital). CAG-kozak-iCre mice (T050269) and *SQSTM1*-KO (T011512) mice were purchased from GemPharmatech. *PDPK1*-cKO mice were generated by crossing CAG-kozak-iCre mice and *PDPK1*$^{fl/fl}$ mice. All of the mice were maintained on a C57BL/6 background and housed in a barrier facility at temperatures of (~20–22 °C) with 50–60% humidity conditions, and all the animal experiments were conducted in accordance with procedures approved by the Animal Ethical and Welfare Committee for Institutional Animal Care and Use Committee (IACUC) of Zhejiang University (approval no. ZJU20220495). The day of birth was considered postnatal day 0 (P0). Mice between 8 and 10 weeks of age were used in the studies.

Genotyping

The genotypes were identified via PCR with genomic DNA obtained from the toes or tails. The sequences of the primers used to identify specific genotypes were as follows: PDPK1$^{fl/fl}$, 5′-CTATGCTGTGTTACTT CTTGGAGCACAG-3′ and 5′-TGTGGACAAACAGCAATGAACATACAC GC-3′; Cre, 5′-CCCAAAGTCGCTCTGAGTTGTTA-3′ and 5′-TTCCTCCTA CATAGTTGGCAGTG-3′; SQSTM1 S1-471-F: 5′-GCTAGTCAAGGGCTCT

ATTTCTG-3′, S1-471-R: 5′-GGTCACAACTGTTCAGTTCTGCC-3′; S1-421-F: 5′-GCCAGGAATTACCTCGATGATAG-3′, and S1-421-R: 5′-AACCAGATG TGGAACTCTCAGC-3′.

Animal experiments

The animal experiments were performed in accordance with the guidelines of the Chinese Council on Animal Care, and the research protocol was approved by the Animal Ethical and Welfare Committee for Institutional Animal Care and Use Committee (IACUC) of Zhejiang University (approval no. ZJU20220495). Six mice (8–10 weeks old) per group were anesthetized via ketamine injection and then intranasally inoculated with sterilized PBS (control) or recombinant VSVs (VSV-GFP, VSV-M, VSV-M$\triangle\beta_{3\text{-}5}$; 5×10^8 p.f.u. per mouse; 50 μL) or H1N1 (7×10^6 p.f.u. per mouse; 60 μL). At 48 h postinfection, the mice were euthanized, and the lungs were isolated. The histopathological analysis of the lung sections was performed via H&E staining, virus titers in the lungs were determined via $TCID_{50}$ assays in Vero E6 or MDCK cells, the viral genome levels in the lungs were measured via RT–qPCR, and the viral protein expression in the lungs was measured by immunoblot analysis.

For treatment with OSU-03012 or the interfering peptide (IM$\beta_{3\text{-}5}$), the mice were pretreated by oral gavage with Cremophor (control) or OSU-03012 (50 mg/kg) or intranasally inoculated with the scrambled peptide (SP) (control) or IM$\beta_{3\text{-}5}$ (25 mg/kg peptide in a 50 μl volume) for 3 continuous days. The mice were infected as described above on the third day. Then, the VSV-M-infected mice were treated with OSU-03012, SP or IM$\beta_{3\text{-}5}$ as described above at 3 h and 24 h after infection. At 48 h postinfection, the mice were euthanized, and the lungs were collected. The histopathological analysis was performed via H&E staining, and viral titers in the lungs were determined via $TCID_{50}$ assays. The viral genome levels and viral load in the lungs were measured via RT–qPCR, and viral protein expression in the lungs was measured by immunoblot analysis.

The mice were infected and treated with SP or the interfering peptide (IM$\beta_{3\text{-}5}$) as described above to observe the survival of mice to determine the survival rate of the mice.

Viral load detection

Absolute quantitative RT–qPCR was used to calculate the number of viral copies to determine the viral load. Total RNA was extracted from the lungs using TRIzol reagent according to the manufacturer's instructions, and DNase I (NEB, M0303) was used to remove DNA. The RNA was reverse transcribed into cDNA using a reverse transcription kit. The vector VSV-G was used as a standard DNA template for calculating the quantity of VSV-GFP, VSV-M or VSV-M$\triangle\beta_{3\text{-}5}$ viral material. Tenfold serial dilutions of plasmids containing VSV-G (1×10^1 to 1×10^{10} template copies per reaction) were analyzed via qPCR, and total viral copies were calculated from Ct values using the resulting standard curves to quantify viral copies in lung tissues or cells. The real-time PCR primers used were as follows:

G-F: 5′- GCCCAAGAGTCACAAGGCTA-3′ and G-R: 5′- CGGTCCAT ACCAGCGGAAAT-3′.

Flow cytometry

The lungs were cut into 2–3 mm pieces and digested in PBS containing 2% FBS and 1 mg/mL collagenase type I at 37 °C for 4 h. After the termination of digestion, a single-cell suspension was obtained by repeated blowing and suction with pipettes and filtration through a 70-μm filter. Following erythrocyte lysis in the lung cell suspensions by incubation with red blood cell lysis buffer, the cells were washed with PBS containing 0.5% FBS and stained with the fluorochrome-labeled antibodies, including anti-CD11c PE-Cy7 (1:200), anti-CD11b BV421 (1:400), anti-Ly6G FITC (1:500), anti-F4/80 PE (1:200), anti-CD4 APC (1:200) and anti-I-A/I-E BV510 (1:500), in PBS containing 0.5% FBS for 15 min on ice. The stained cells were analyzed with a BD FACSVerse™ flow cytometer using BD FACSuite™ (v 1.3.0). The data were analyzed and visualized using FlowJo10.8.1.

Lung histology and immunofluorescence staining

Lungs from control or virus-infected mice were dissected, fixed with 10% phosphate-buffered formalin, embedded in paraffin, sectioned, stained with H&E solution and examined under a light microscope to analyze histological changes. Transverse sections (5 μm) were dewaxed and rehydrated. Antigen retrieval was performed using hot citric acid buffer treatment (10 mM citric acid, pH 6.0). For immunofluorescence staining, the sections were incubated with an anti-FITC primary antibody overnight at 4 °C. The tissue sections were stained with an Alexa Fluor 488-conjugated secondary antibody for 1 h at room temperature, washed and mounted with DAPI. Fluorescence images were captured with a Carl Zeiss scanning microscope. Then, the tissue sections were counterstained with hematoxylin and eosin (H&E) to analyze histological changes with a Carl Zeiss scanning microscope.

Statistical analysis

For western blot analysis, protein bands were quantified by measuring the mean gray value of the bands within the linear range and background using FIJI (v 2.3.0). The quantification represents the relative amounts, which are presented as the ratio of each net band value to the net loading control. Statistical significance was determined using unpaired two-tailed Student's t test and two-way ANOVA by Graphpad 6.01. The results from three independent biological experiments are presented as the means ± SEM. Significance was determined at a P value of 0.05 or less. No exclusions of data points or mice occurred, and randomization or blinding methods were not employed.

Reporting summary

Further information on research design is available in the Nature Portfolio Reporting Summary linked to this article.

Data availability

The protein mass spectrometry raw data generated in this study have been deposited in Integrated Proteome Resources under accession code PXD049167. Source data are provided with this paper.

References

1. Gu, W. J. et al. The molecular mechanism of SARS-CoV-2 evading host antiviral innate immunity. *Virol. J.* **19**, 49 (2022).
2. Rashid, F. et al. Roles and functions of SARS-CoV-2 proteins in host immune evasion. *Front. Immunol.* **13**, 940756 (2022).
3. Bonilauri, P. & Rugna, G. Animal coronaviruses and SARS-COV-2 in animals, what do we actually know? *Life* **11**, 123 (2021).
4. Shan, T. J., Li, L. Y., Yang, J. M. & Cheng, Y. Role and clinical implication of autophagy in COVID-19. *Virol. J.* **20**, 125 (2023).
5. Chen, T. et al. The role of autophagy in viral infections. *J. Biomed. Sci.* **30**, 5 (2023).
6. Zhu, L. Q., Mou, C. X., Yang, X., Lin, J. & Yang, Q. Mitophagy in TGEV infection counteracts oxidative stress and apoptosis. *Oncotarget* **7**, 27122–27141 (2016).
7. Li, X. Y. et al. SARS-CoV-2 ORF10 suppresses the antiviral innate immune response by degrading MAVS through mitophagy (vol 19, pg 67, 2022). *Cell Mol. Immunol.* **20**, 686–686 (2023).
8. Tian, G. M. et al. Baicalin mitigates nephropathogenic infectious bronchitis virus infection-induced spleen injury via modulation of mitophagy and macrophage polarization in Hy-Line chick. *Vet. Microbiol.* **286**, 109891 (2023).
9. Zong, S. et al. SARS-CoV-2 Nsp8 induces mitophagy by damaging mitochondria. *Virol. Sin.* **38**, 520–530 (2023).
10. Li, X. et al. TRIM28 promotes porcine epidemic diarrhea virus replication by mitophagy-mediated inhibition of the JAK-STAT1 pathway. *Int. J. Biol. Macromol.* **254**, 127722 (2024).

11. Zhai, X. Y. et al. N protein of PEDV plays chess game with host proteins by selective autophagy. *Autophagy* **19**, 2338–2352 (2023).
12. Fu, Y. A. et al. mLST8 is essential for coronavirus replication and regulates its replication through the mTORC1 pathway. *Mbio* **14**, e0089923 (2023).
13. Gao, Q. et al. KPNA2 suppresses porcine epidemic diarrhea virus replication by targeting and degrading virus envelope protein through selective autophagy. *J. Virol.* **97**, e0011523 (2023).
14. Choi, Y., Bowman, J. W. & Jung, J. U. Autophagy during viral infection - a double-edged sword. *Nat. Rev. Microbiol.* **16**, 340–353 (2018).
15. Vargas, J. N. S., Hamasaki, M., Kawabata, T., Youle, R. J. & Yoshimori, T. The mechanisms and roles of selective autophagy in mammals. *Nat. Rev. Mol. Cell Biol.* **24**, 167–185 (2023).
16. Sanchez-Martin, P. & Komatsu, M. p62/SQSTM1 - steering the cell through health and disease. *J. Cell Sci.* **131**, jcs222836 (2018).
17. Orvedahl, A. et al. Autophagy protects against sindbis virus infection of the central nervous system. *Cell Host Microbe* **7**, 115–127 (2010).
18. Aparicio, R., Hansen, M., Walker, D. W. & Kumsta, C. The selective autophagy receptor SQSTM1/p62 improves lifespan and proteostasis in an evolutionarily conserved manner. *Autophagy* **16**, 772–774 (2020).
19. Orvedahl, A. et al. Image-based genome-wide siRNA screen identifies selective autophagy factors. *Nature* **480**, 113–117 (2011).
20. Hui, X. F. et al. SARS-CoV-2 promote autophagy to suppress type I interferon response. *Signal Transduct. Tar.* **6**, 180 (2021).
21. De Duve, C. & Wattiaux, R. Functions of lysosomes. *Annu. Rev. Physiol.* **28**, 435–492 (1966).
22. Vats, A. et al. Poly I:C stimulation in-vitro as a marker for an antiviral response in different cell types generated from Buffalo (Bubalus bubalis). *Mol. Immunol.* **121**, 136–143 (2020).
23. Liu, Y. S. et al. Targeting selective autophagy as a therapeutic strategy for viral infectious diseases. *Front. Microbiol.* **13**, 889835 (2022).
24. Nixon, R. A. The role of autophagy in neurodegenerative disease. *Nat. Med.* **19**, 983–997 (2013).
25. Pan, T. H., Kondo, S., Le, W. D. & Jankovic, J. The role of autophagy-lysosome pathway in neurodegeneration associated with Parkinson's disease. *Brain* **131**, 1969–1978 (2008).
26. Menzies, F. M., Fleming, A. & Rubinsztein, D. C. Compromised autophagy and neurodegenerative diseases. *Nat. Rev. Neurosci.* **16**, 345–357 (2015).
27. White, E. Deconvoluting the context-dependent role for autophagy in cancer. *Nat. Rev. Cancer* **12**, 401–410 (2012).
28. Degenhardt, K. et al. Autophagy promotes tumor cell survival and restricts necrosis, inflammation, and tumorigenesis. *Cancer Cell* **10**, 51–64 (2006).
29. Singh, R. et al. Autophagy regulates lipid metabolism. *Nature* **458**, 1131–U1164 (2009).
30. Ebato, C. et al. Autophagy is important in islet homeostasis and compensatory increase of beta cell mass in response to high-fat diet. *Cell Metab.* **8**, 325–332 (2008).
31. Booth, L. et al. GRP78/BiP/HSPA5/Dna K is a universal therapeutic target for human disease. *J. Cell Physiol.* **230**, 1661–1676 (2015).
32. Rayner, J. O. et al. AR12 (OSU-03012) suppresses GRP78 expression and inhibits SARS-CoV-2 replication. *Biochem. Pharm.* **182**, 114227 (2020).
33. Booth, L. et al. Regulation of OSU-03012 toxicity by ER stress proteins and ER stress-inducing drugs (Publication with Expression of Concern. See vol. 18, pg. 1669, 2019). *Mol. Cancer Ther.* **13**, 2384–2398 (2014).
34. Booth, L. et al. OSU-03012 and viagra treatment inhibits the activity of multiple chaperone proteins and disrupts the blood-brain barrier: implications for anti-cancer therapies. *J. Cell Physiol.* **230**, 1982–1998 (2015).
35. Roberts, J. L. et al. GRP78/Dna K is a target for nexavar/stivarga/votrient in the treatment of human malignancies, viral infections and bacterial diseases. *J. Cell Physiol.* **230**, 2552–2578 (2015).
36. Booth, L. et al. AR-12 inhibits multiple chaperones concomitant with stimulating autophagosome formation collectively preventing virus replication. *J. Cell Physiol.* **231**, 2286–2302 (2016).
37. Chan, J. F. W. et al. The celecoxib derivative kinase inhibitor AR-12 (OSU-03012) inhibits Zika virus via down-regulation of the PI3K/Akt pathway and protects Zika virus infected A129 mice: a host-targeting treatment strategy. *Antivir. Res.* **160**, 38–47 (2018).
38. Medzhitov, R. & Janeway, C. A. Jr Innate immune recognition and control of adaptive immune responses. *Semin. Immunol.* **10**, 351–353 (1998).
39. Desforges, M. et al. Different host-cell shutoff strategies related to the matrix protein lead to persistence of vesicular stomatitis virus mutants on fibroblast cells. *Virus Res.* **76**, 87–102 (2001).

Acknowledgements

We thank Zhong-Zhou Yang from the State Key Laboratory of Pharmaceutical Biotechnology, Department of Cardiology, Nanjing Drum Tower Hospital, for kindly providing the *PDPK1*$^{fl/fl}$ mice. This study was supported by the National Key Research and Development Programs of China (2021YFD1801102), the National Natural Science Foundation of China (32172863), the Fundamental Research Funds for the Central Universities (2022-KYY-517101-0005) and Hangzhou Chengxi Sci-tech innovation Corridor Management Committee. We thank Wei Yin from the Core Facilities, Zhejiang University School of Medicine, and Yuchen Zhang from the Center of Cryo-Electron Microscopy (CCEM), Zhejiang University for their technical support.

Author contributions

Boli Hu, Jiyong Zhou and Yahui Li conceived of, designed and wrote the manuscript for this project. Boli Hu and Jiyong Zhou provided supervision and project administration and secured financial support.Yahui Li, Chunyan Li and Chenchen Zhao led cell-based and animal, tissue in vivo and in vitro molecular experiments and data analyzes. Yahui Li, Chunyan Li, Chenchen Zhao, Jiayu Wu, Ya Zhu, Fei Wang and Jiepeng Zhong performed cell-based and animal, tissue in vivo and in vitro molecular experiments and data analyzes. Yan Yan, Yulan Jin, Weiren Dong, Jinyang Chen and Xianghong Yang participated in the discussion of the results and provided technical and resource support. Boli Hu reviewed the manuscript for intellectual content. Yahui Li, Jiyong Zhou and Boli Hu revised the manuscript for intellectual content.

Competing interests

The authors declare no competing interests

Additional information

Supplementary information The online version contains supplementary material available at https://doi.org/10.1038/s41467-024-53100-z.

Correspondence and requests for materials should be addressed to Jiyong Zhou or Boli Hu.

Peer review information *Nature Communications* thanks Meng-Qiu Dong and the other, anonymous, reviewer(s) for their contribution to the peer review of this work. A peer review file is available.